Article

Cell Reports

m^{6}A RNA Methylation Maintains Hematopoietic Stem Cell Identity and Symmetric Commitment

Graphical Abstract

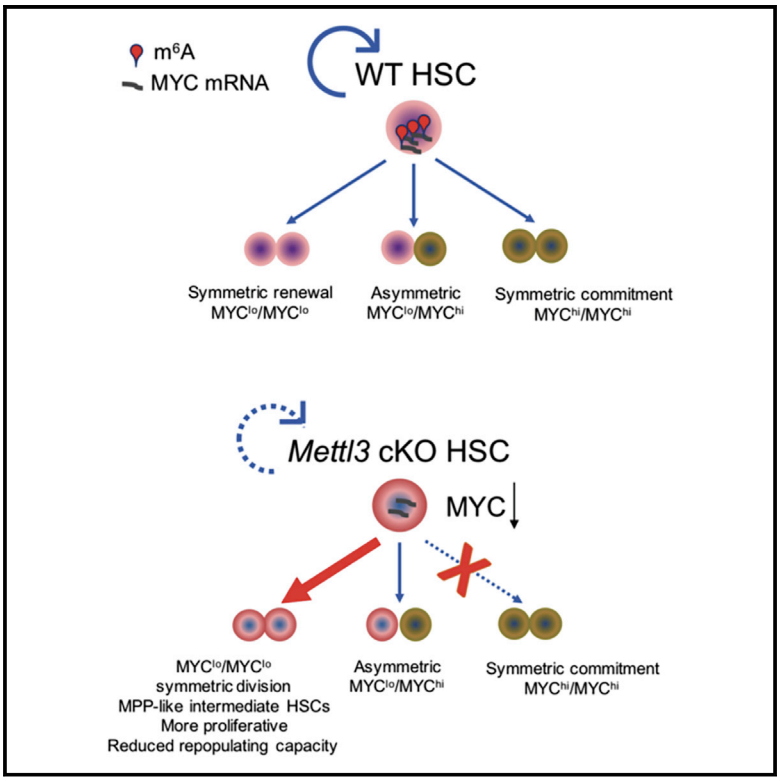

Highlights

- Single-cell RNA-seq uncovers an HSC-MPP intermediate population after m^{6}A depletion
- m^{6}A-depleted HSC-MPPs molecularly and functionally resemble normal MPPs
- m^{6}A controls HSC symmetric commitment and identity through MYC mRNA stability
- Asymmetric segregation of MYC during HSC division provides a marker for commitment

Authors

Yuanming Cheng, Hanzhi Luo, Franco Izzo, ..., Samie R. Jaffrey, Dan A. Landau, Michael G. Kharas

Correspondence

dal3005@med.cornell.edu (D.A.L.), kharasm@mskcc.org (M.G.K.)

In Brief

Cheng et al. uncover RNA methylation as a guardian in hematopoietic stem cell (HSC) fate decisions. m^{6}A maintains hematopoietic stem cell symmetric commitment and identity. This study may provide a general mechanism for how RNA methylation controls cellular fate.

Cheng et al., 2019, Cell Reports *28*, 1703–1716
August 13, 2019
https://doi.org/10.1016/j.celrep.2019.07.032

CellPress

Cell Reports
Article

m^{6}A RNA Methylation Maintains Hematopoietic Stem Cell Identity and Symmetric Commitment

Yuanming Cheng,[1,9] Hanzhi Luo,[1,7] Franco Izzo,[2,3,7] Brian F. Pickering,[4] Diu Nguyen,[1] Robert Myers,[2,3] Alexandra Schurer,[1] Saroj Gourkanti,[1] Jens C. Brüning,[5] Ly P. Vu,[1,6,7] Samie R. Jaffrey,[4] Dan A. Landau,[2,3,8,*] and Michael G. Kharas[1,10,*]

[1]Molecular Pharmacology Program, Center for Cell Engineering, Center for Stem Cell Biology, Center for Experimental Therapeutics, Center for Hematologic Malignancies, Memorial Sloan Kettering Cancer Center, New York, NY, USA
[2]New York Genome Center, New York, NY, USA
[3]Meyer Cancer Center, Weill Cornell Medicine, New York, NY, USA
[4]Department of Pharmacology, Weill Cornell Medicine, Cornell University, New York, NY, USA
[5]Department of Mouse Genetics and Metabolism, Institute for Genetics and Center for Molecular Medicine (CMMC), University of Cologne, Zülpicher Strasse 47b, 50674 Cologne, Germany
[6]Terry Fox Laboratory, British Columbia Cancer Research Centre, Vancouver, BC, Canada
[7]Molecular Biology and Biochemistry, Simon Fraser University, Vancouver, BC, Canada
[8]Institute of Computational Biomedicine, Weill Cornell Medicine, New York, NY, USA
[9]These authors contributed equally
[10]Lead Contact
*Correspondence: dal3005@med.cornell.edu (D.A.L.), kharasm@mskcc.org (M.G.K.)
https://doi.org/10.1016/j.celrep.2019.07.032

SUMMARY

Stem cells balance cellular fates through asymmetric and symmetric divisions in order to self-renew or to generate downstream progenitors. Symmetric commitment divisions in stem cells are required for rapid regeneration during tissue damage and stress. The control of symmetric commitment remains poorly defined. Using single-cell RNA sequencing (scRNA-seq) in combination with transcriptomic profiling of HSPCs (hematopoietic stem and progenitor cells) from control and m^{6}A methyltransferase *Mettl3* conditional knockout mice, we found that m^{6}A-deficient hematopoietic stem cells (HSCs) fail to symmetrically differentiate. Dividing HSCs are expanded and are blocked in an intermediate state that molecularly and functionally resembles multipotent progenitors. Mechanistically, RNA methylation controls *Myc* mRNA abundance in differentiating HSCs. We identified MYC as a marker for HSC asymmetric and symmetric commitment. Overall, our results indicate that RNA methylation controls symmetric commitment and cell identity of HSCs and may provide a general mechanism for how stem cells regulate differentiation fate choice.

INTRODUCTION

Hematopoietic stem cells (HSCs) balance their long-lived regenerative capacity with the ability to maintain myeloid, lymphoid, and erythroid lineage output in the blood. This balance is mediated through cell fate decisions that occur during cellular division. When they divide, HSCs either self-renew or undergo differentiation toward a multipotent progenitor cell (MPP) fate, where the cells are metabolically more active than HSCs and retain multi-lineage potency but lack HSC-long-term engraftment activity. The choice between these distinct cellular outcomes is controlled by the ability to alternate between a symmetric or asymmetric fate choice (Knoblich, 2008; Morrison and Kimble, 2006). It remains unclear what signals can determine whether a cellular division leads to cellular commitment (differentiation) or self-renewal. Mechanistic insights into the regulation of cell fate decisions may inform approaches to bone marrow failure syndromes, differentiation therapy of hematopoietic malignancies, and stem cell expansion for therapeutic benefits.

A key controller of cellular fate is mRNA methylation. The most common reversible posttranscriptional mRNA modification on mRNA is N^6-methyladenosine (m^{6}A). The presence of m^{6}A alters mRNA metabolism, including mRNA stability, mRNA splicing, and translation efficiency (Coots et al., 2017; Meyer and Jaffrey, 2017; Meyer et al., 2015; Ping et al., 2014; Roundtree et al., 2017; Schwartz et al., 2014; Slobodin et al., 2017; Wang et al., 2015; Xiao et al., 2016). The deposition of transcriptome-wide m^{6}A marks depends on the METTL3-METTL14-WTAP-VIRMA-ZC3H13-RBM15 protein complex, in which METTL3 serves as the catalytic subunit. m^{6}A controls cell state maintenance in a cellular-context-dependent manner. Embryonic stem cells (ESCs) with *Mettl3* deficiency remain naive and fail to differentiate into primed ESCs (Batista et al., 2014; Geula et al., 2015) and specification of hematopoietic stem and progenitor cells (HSPCs) requires METTL3 in zebrafish and mouse embryos (Lv et al., 2018; Zhang et al., 2017).

A number of recent studies showed that m^{6}A and METTL3 are important for survival and maintenance of the undifferentiated stages of myeloid leukemia cells (Barbieri et al., 2017; Vu et al., 2017a; Weng et al., 2018). However, as therapeutics toward METTL3 are being developed to target myeloid leukemia

(Boriack-Sjodin et al., 2018), it is important to understand how loss of m^{6}A affects normal blood development. Several studies have reported that disruption of m^{6}A regulators impacts normal HSC function. Depletion of YTHDF2, a m^{6}A reader protein, results in increased HSCs that are capable of normal engraftment, while loss of writer protein METTL3 leads to an accumulation of HSCs with impaired differentiation capacity and normal self-renewal (Lee et al., 2019; Li et al., 2018; Yao et al., 2018). However, the mechanism by which m^{6}A affects HSC expansion remains unknown. Additionally, MYC was reported as a major target of m^{6}A that contributes to the effects of m^{6}A in myeloid leukemia and in HSCs (Lee et al., 2019; Vu et al., 2017a) However, it remains unclear if m^{6}A simply alters MYC expression, or if m^{6}A has other regulatory roles that mediate MYC's effects in HSC accumulation.

To understand how m^{6}A shapes the early differentiation decisions during hematopoietic differentiation, we performed single-cell RNA sequencing (RNA-seq) in wild-type (WT) and *METTL3* knockout hematopoietic progenitor cells. In contrast to the HSC accumulation phenotype that has been described upon *METTL3* depletion previously, we report here that HSCs are instead depleted. We show that the expanded population is not in the HSC pool but, instead, comprises a HSC-like intermediate state that molecularly and functionally resembles multipotent progenitors. Mechanistically, we show that m^{6}A is required for HSCs' symmetric commitment step in hematopoietic differentiation, with normal asymmetric commitment upon METTL3 depletion. We find that m^{6}A controls *Myc* RNA stability and this m^{6}A-regulated expression of *Myc* controls HSC symmetric commitment. The HSC-like intermediate population that is metabolically activated but fails to symmetrically commit has uncoupled the role for MYC in HSC activation and cellular commitment. Our data advance the concepts that m^{6}A is essential for HSC identity maintenance and it tightly controls HSCs entry toward commitment. Overall, we find that the major role for m^{6}A in hematopoietic differentiation is due to its ability to regulate symmetric commitment via controlling *Myc* mRNA stability.

RESULTS

Mettl3 Is Required for Normal Hematopoiesis

To study the role of m^{6}A in normal hematopoiesis and cellular fate, we crossed the *Mettl3 flox/flox* (*Mettl3 f/f*) mice with the *Mx1-Cre* mice to generate *Mettl3 f/f*, *Mx1-Cre*$^+$ conditional knockout (*cKO*) mice (Figure 1A). *Mettl3* depletion was then induced by injection with polyinosinic-polycytidylic acid (pIpC) (Figure S1A). Analysis of pIpC-treated *Mettl3 f/f*, *Mx1-Cre*$^+$ *(Mettl3 cKO)* and control *Mettl3 f/f*, *Mx1-Cre*$^-$ *(Mettl3 f/f)* confirmed efficient *Mettl3* genomic deletion (Figure 1B) and ablation of METTL3 protein in HSPCs (LSK, Lineage$^-$ cKit$^+$Sca-1$^+$) (Figure S1B). We further confirmed that the loss of METTL3 reduced global m^{6}A levels in bone marrow cells (Figure 1C).

We then evaluated the hematopoietic system upon depletion of *Mettl3* and global m^{6}A. We observed in *Mettl3 cKO* mice a 40% reduction in bone marrow cellularity and pancytopenia (Figures 1D and 1E). Flow analysis of bone marrow cells from *Mettl3 cKO* mice revealed a marked reduction in Gr1$^+$Mac1$^+$ mature granulocyte and Ter119$^+$CD71^{med} /Ter119$^+$CD71^{low} (Ery3/Ery4) erythroid cells (Figures S1C and S1D), as well as an increase in CD41$^+$ megakaryocytes (Figure S1C) without major defects in lymphoid lineages compared to control mice (Figure S1E). Analysis of bone marrow sections confirmed that *Mettl3 cKO* mice had reduced mature granulocytes and increased immature myeloid cells (Figure S1F). Histopathological analysis in *Mettl3 cKO* mice further showed dysplasia in megakaryocytes characterized by abnormal micromegakaryocytes with a large fraction characterized with monolobated megakaryocytes, a feature associated with altered differentiation (Figure S1F). Moreover, METTL3-depleted bone marrow cells demonstrated a significant reduction in the ability to proliferate and differentiate to form myeloid colonies *in vitro* (Figure S1G). Additionally, *Mettl3 cKO* mice exhibited enlarged spleens with extensively infiltrated red pulp zones and perturbed splenic architecture, which is associated with an accumulation of immature erythroblasts at the expense of B and T cells (Figures S1H–S1K). Taken together, these data indicated an impairment in maturation and terminal differentiation of myeloid and erythroid lineages upon METTL3 ablation and reduction of m^{6}A.

Given the broad, multi-lineage defects of METTL3 loss in the hematopoietic system, we hypothesized that the defects originate from the hematopoietic stem and progenitor compartments. The HSPC compartment can be further defined using cell surface markers (i.e., SLAM/CD150 and CD48) into HSCs (LSK, CD150$^+$CD48$^-$) and MPPs. MPPs, which all have short-term stem cell activity, can be subdivided into three populations: MPP1s, which are considered unbiased (LSK, CD150$^-$CD48); MPP2s, which have a bias toward megakaryocytic and erythroid lineages (LSK, CD150$^+$CD48$^+$); and MPP4s, with lymphoid lineage bias (LSK, CD150$^-$CD48$^+$) (Kiel et al., 2005; Oguro et al., 2013; Rodriguez-Fraticelli et al., 2018). We examined all four populations and observed a 5-fold increase in the frequency of HSPCs (LSKs) and a nearly 10-fold expansion in immunophenotypic HSCs, as well as MPP2s and MPP4s in the bone marrow of *Mettl3 cKO* mice as compared to control *Mettl3 f/f* mice (Figures 1F and 1G). Notably, the MPP1 subset of MPPs was not increased in *Mettl3 cKO* mice. However, the downstream myeloid progenitors (MPs, Lin$^-$ckit$^+$Sca-1$^-$) comprising common myeloid progenitors (CMP; Lin$^-$cKit$^+$Sca-1$^-$CD34$^+$FcrR$^-$) and granulocyte myeloid progenitors (GMP; Lin$^-$cKit$^+$Sca-1$^-$CD34$^+$FcrR$^+$) were significantly reduced in *Mettl3 cKO* mice (Figure S1L). Overall, these data suggested that loss of m^{6}A imposed a blockage in transition of HSCs to MPs, thereby hindering commitment of HSCs toward a myeloid fate.

To explore the dosage effect of *Mettl3* loss on hematopoiesis, we evaluated heterozygous *Mettl3 f/–*, *Mx1-Cre+ (Het*, *Cre+)* mice. Similar to the control mice, heterozygous *Mettl3* deletion had equivalent bone marrow (BM) cellularity and peripheral blood counts (white blood cells [WBCs], red blood cells [RBCs], and platelets) 3 weeks post-deletion (Figures S2A and S2B). However, we found that the *Mettl3* het mice also exhibited splenomegaly, which was associated with an accumulation of erythroid blasts and reduction of T cells (Figures S2C and S2D). Moreover, HSCs were also expanded in the *Mettl3* het mice while the downstream lymphoid, myeloid, and erythroid populations were equivalent to controls except for the reduction in the pre-pro B cell population in the *Mettl3* het mice (Figures S2E–S2H). These data suggest an intermediate dose requirement for *Mettl3* in normal hematopoiesis.

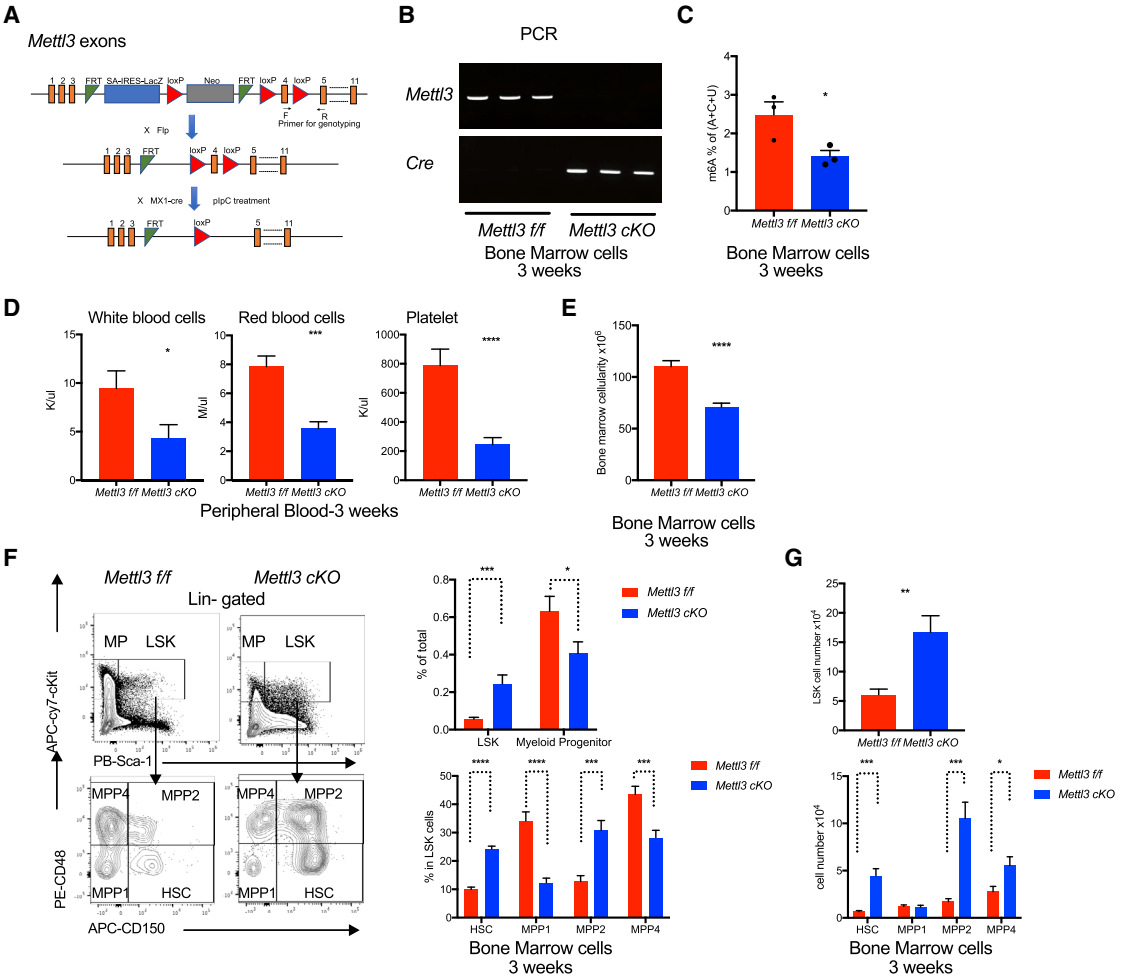

Figure 1. Expansion of HSCs in *Mettl3* cKO Mice

(A) Target scheme for *Mettl3* conditional knockout (cKO) mice. Primers were designed for genotyping by targeting *Mettl3* exon 4.

(B) Successful deletion of *Mettl3* in the cKO bone marrow 3 weeks post-pIpC injections. PCR by using genomic DNA from pIpC-treated mice bone marrow cells to validate *Mettl3* exon4 deletion and *Cre* expression. Primers used were indicated in (A).

(C) Decreased m^6A in cKO mice 3 weeks post-pIpC. Global m6A levels in *Mettl3* f/f and *Mettl3* cKO BM cells were measured by two-dimensional thin-layer chromatography (TLC). n = 3.

(D) *Mettl3 cKO* mice developed a pancytopenia phenotype 3 weeks post-pIpC. Whole blood counts of white blood cell (WBCs), red blood cells (RBCs), and platelets (PLT) of *Mettl3 f/f* and *Mettl3 cKO* mice. n = 11.

(E) Reduction in bone marrow cellularity in *cKO* mice 3 weeks post-pIpC. Bone marrow cellularity of *Mettl3 f/f* and *Mettl3 cKO* mice was determined. n = 11.

(F) Left: representative flow cytometry plots for gating strategies of hematopoietic stem and progenitor cell (HSPC) compartments. An expansion in HSPC population and a reduction in myeloid progenitors upon *Mettl3* depletion. Right top: frequency of LSK ($Lin^-cKit^+Sca\text{-}1^+$) and MP (Myeloid progenitor, $Lin^-cKit^+Sca\text{-}1^-$) in BM cells. Right bottom: percentage of HSC (LSK, $CD150^+CD48^-$), MPP1 (LSK, $CD150^-CD48^-$), MPP2 (LSK, $CD150^+CD48^+$), and MPP4 (LSK, $CD150^-CD48^+$) in LSK population. n = 11.

(G) Absolute cell numbers of LSKs, HSCs, and MPPs in *Mettl3* f/f and *Mettl3* cKO mice at 3 weeks post-pIpC injection. n = 11. Mean and SEM are shown (*$p < 0.05$, **$p < 0.01$, ***$p < 0.001$, and ****$p < 0.0001$). n represents number of mice.

Mettl3-Depleted HSCs Are More Activated and Functionally Defective in Reconstitution

As we observed defects in progenitor pools and mature lineages with an expansion of HSCs upon METTL3 depletion, we hypothesized that m^6A is critical to maintain HSC function. We first examined whether loss of m^6A results in the exit of quiescence in HSCs. Under normal homeostatic conditions, a majority of HSCs remain dormant in G_0 while a fraction of HSCs enter cell cycle to divide and generate progenitor cells (Attar and Scadden, 2004). Loss of *Mettl3* results in an increased frequency of cells that have exited G_0 and increased percentage of cells that are actively dividing (Figures 2A, 2B, and S2I). These proliferative HSCs with depleted *Mettl3* are also metabolically activated, with increased mitochondrial mass and activity (Figures 2C, 2D, and S2J). Consistent with previous findings that loss of quiescence in HSCs is attributed to reduced engrafting potential

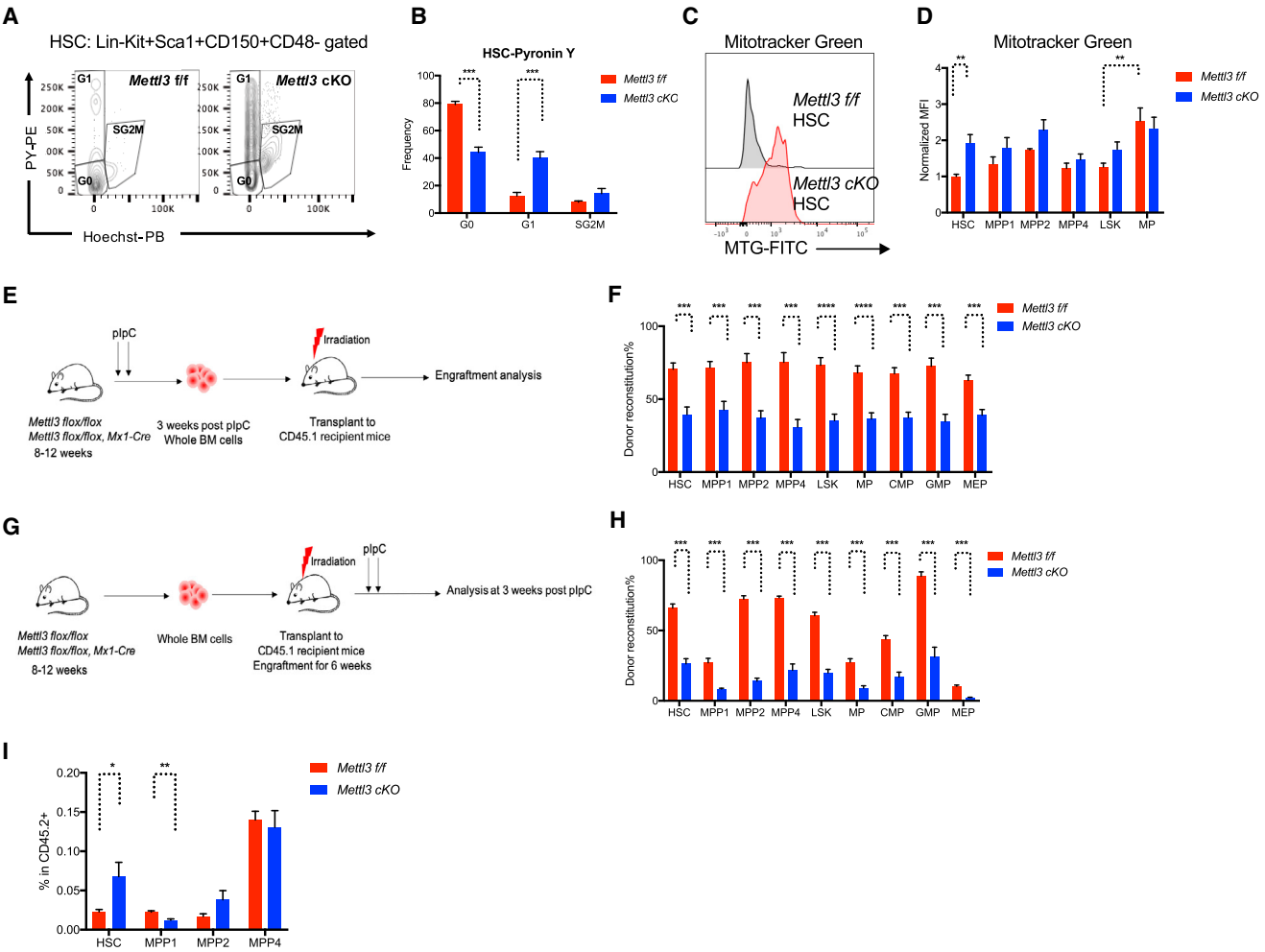

Figure 2. *Mettl3 cKO* HSCs Are Less Quiescent and Functionally Defective

(A) *Mettl3* cKO HSCs are less quiescent. Representative flow cytometry plots for assessing cell cycle status of *Mettl3* f/f and *Mettl3* cKO HSC by Pyronin Y staining.

(B) Quantification of cell cycle analysis. n = 5.

(C) Increased mitochondrial mass in *Mettl3 cKO* HSCs. Representative histograms of Mitotracker Green staining in *Mettl3 f/f* and *Mettl3 cKO* HSCs.

(D) Mitochondrial mass of different HSPC population was evaluated by Mitotracker Green staining quantified by flow cytometry. n = 5.

(E) Scheme of transplant strategy. Non-competitive reconstitution assay in which 10^6 donor BM cells from *Mettl3 f/f* or *Mettl3 cKO* mice at 3 weeks post-pIpC were transplanted into CD45.1 congenic recipient mice.

(F) *Mettl3 cKO* bone marrow fails to reconstitute hematopoietic compartments in recipient mice. CD45.2 chimerisms of HSCs, MPPs and progenitor compartments from (E) were analyzed by flow cytometry at 16 weeks post-transplant. n = 10.

(G) Scheme of the experimental procedure in (H) and (I). CD45.1 recipient mice were transplanted with *Mettl3 flox/flox Cre*$^-$ or *Cre*$^+$ bone marrow cells (pre-pIpC). At 6 weeks post-transplantation, CD45.1 congenic recipient mice were then injected with pIpC to deplete METTL3.

(H) The reconstitution defect in *Mettl3 cKO* bone marrow is cell-autonomous. CD45.2 chimerism analysis of HSCs, MPPs, and progenitor compartments from experiment (G) at 3 weeks post-pIpC. n = 5.

(I) Frequencies of HSCs and MPPs in the donor CD45.2 population from experiment (G). n = 5. Mean and SEM are shown (*p < 0.05, **p < 0.01, ***p < 0.001, and ****p < 0.0001). n represents number of mice.

(Cheng et al., 2000; Hock et al., 2004), *Mettl3 cKO* bone marrow cells exhibited a significant defect in *in vivo* repopulating capacity, characterized by reduced chimerism of all HSPC compartments and mature lineage populations in recipient mice (Figures 2E, 2F, S2K, and S2L). These results indicated that m^{6}A is functionally required for maintaining HSC quiescence and self-renewal potential. The data also suggested that the expansion of HSCs is possibly due to the accumulation of dividing HSCs, incapable of properly differentiating.

To determine if the expansion of *Mettl3*-depleted HSCs and their defective ability to reconstitute the hematopoietic system was cell autonomous and not due to loss of RNA methylation in the heterogeneous niche environment, we engrafted bone marrow cells from both *Mettl3 f/f*, *Mx1-Cre*$^-$ and *Mettl3 f/f*,

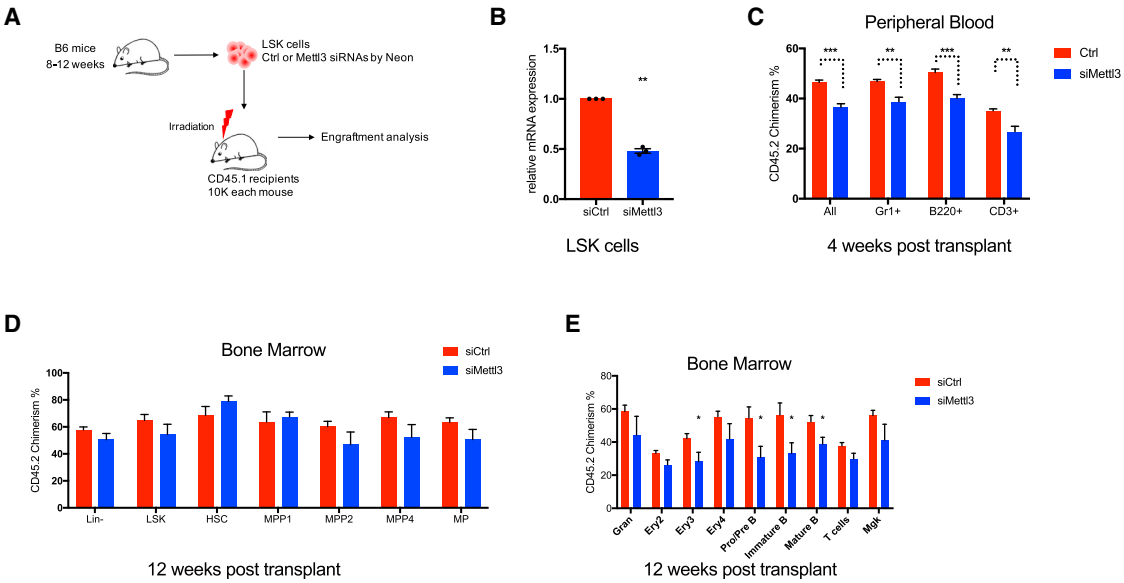

Figure 3. Acute Depletion of *Mettl3* Leads to a Reversible Defect in HSC Repopulating Capacity

(A) Experimental scheme for acute knockdown of *Mettl3* in LSK cells by siRNA followed by transplantation.

(B) qRT-PCR of *Mettl3* to confirm the knockdown efficiency in LSK cells from (A).

(C) Donor engraftments of CD45.2 in different lineage compartments were analyzed by flow cytometry in peripheral blood at 4 weeks post-transplant from (A). ctrl n = 10; siMettl3 n = 5.

(D) CD45.2 chimerism analysis of HSCs, MPPs, and progenitor compartments in bone marrow from experiment (A) at 12 weeks post-transplant. ctrl n = 10; siMettl3 n = 5.

(E) CD45.2 chimerism analysis of different lineage populations in bone marrow from experiment (A) at 12 weeks post-transplant. ctrl n = 10; siMettl3 n = 5. Mean and SEM are shown (*p < 0.05, **p < 0.01, ***p < 0.001, and ****p < 0.0001). n represents number of mice.

Mx1-Cre^{+} mice (Figure 2G), and then depleted *Mettl3* following engraftment through pIpC administration. Donor reconstitution was comparable between *Mettl3 f/f*, *Mx1-Cre*$^{-}$ and *Mettl3 f/f*, *Mx1-Cre*$^{+}$ mice before pIpC treatment (Figure S2M). However, the chimerism of donor engraftment was significantly decreased in the HSPC compartments and in mature lineages 3 weeks after METTL3 depletion (Figures 2H and S2N). Importantly, the expansion of HSCs following METTL3 depletion was recapitulated within the donor population (Figure 2I). These results strongly supported a cell-intrinsic role of METTL3 and m^{6}A in regulating HSC numbers and function.

Next, we sought to determine if alteration in function of *Mettl3 cKO* HSCs is sustained after long-term engraftment (16 weeks post-pIpC), in which MPPs and other differentiated cell types are replenished from their precursors. Similar to acute deletion, the METTL3-depleted HSPCs remained expanded (HSC, MPP2, and MPP4) and demonstrated reduced RBCs in the primary *Mettl3* cKO mice (Figures S3A–S3C). However, defects in downstream lineages were normalized in *Mettl3 cKO* mice, as characterized by normal bone marrow cellularity, WBCs, and mature lineages (Figures S3D–S3H). Splenomegaly was also observed in *Mettl3 cKO* mice with increased immature erythroblasts, even though the reductions of B and T cells were recovered (Figures S3I–S3K). These data were explained by genomic PCR analysis of bone marrow cells, demonstrating an emergence of a WT *Mettl3* population (Figure S3L). Furthermore, these data suggest a strong selective pressure against the loss of RNA methylation during myeloid and lymphoid lineage restriction and the sustained increase in the numbers of METTL3-depleted HSCs suggested a continuous block in the ability of HSCs to differentiate to more committed lineage restricted cells.

Acute Depletion of *Mettl3* Leads to a Reversible Defect in HSC Repopulating Capacity

Targeting METTL3 is a potential therapeutic strategy in acute myeloid leukemia (AML) (Barbieri et al., 2017; Vu et al., 2017a). Prolonged genetic ablation of METTL3 disrupts adult hematopoiesis *in vivo* in a dose-dependent manner. However, it remains unclear whether the effects of METTL3 inhibition on normal HSCs are reversible. Thus, we examined the effect of acute *Mettl3* inhibition on hematopoiesis by transient small interfering RNA (siRNA) knockdown (Figure 3A). Sorted LSK cells were transfected with control or *Mettl3* siRNA and then injected into recipient mice (Figure 3B). Pan hematopoietic donor reconstitution was significantly but modestly reduced in the *Mettl3* knockdown group at a short-term time point (4 weeks) (Figure 3C). However, the engraftment defect induced by acute *Mettl3* loss was normalized in the HSPC compartments at 12 weeks post-transplant (Figure 3D). The chimerism of donor engraftment of the *Mettl3* knockdown group was also comparable to the control group in myeloid, T cell, and megakaryocytes lineages with modest reductions on the erythroid and B cell compartment (Figure 3E). These data suggest that acute inhibition of *Mettl3* could induce a reversible defect in normal hematopoiesis. Together

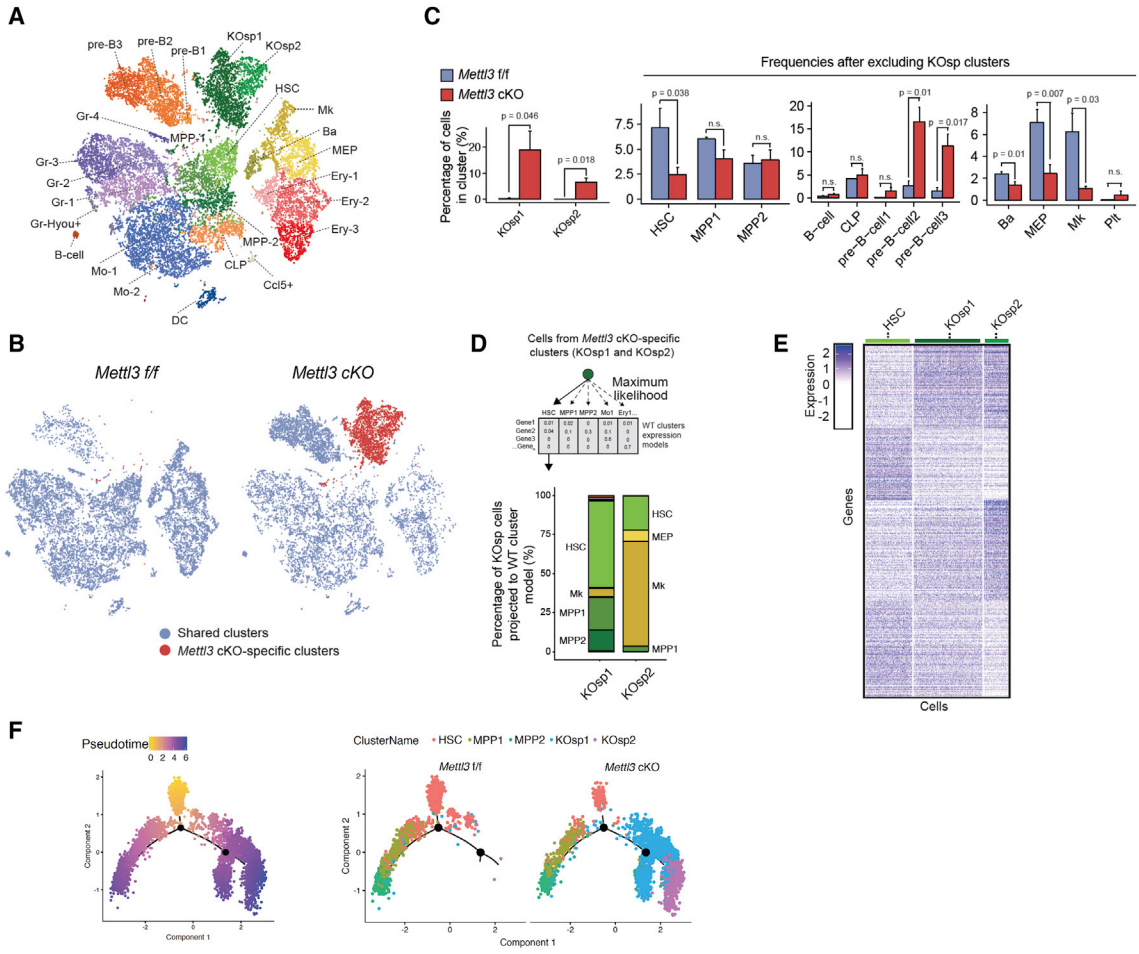

Figure 4. *Mettl3* Deletion Results in a Defect in Lineage Commitment and the Development of Two Distinct HSC-like Populations

(A) Identification of different hematopoietic clusters in *Mettl3 f/f* and *Mettl3 cKO* Lineage$^-$cKit$^+$ cells base on tSNE analysis from single-cell RNA sequencing (scRNA-seq).

(B) Two specific clusters in *Mettl3 cKO* Lin$^-$cKit$^+$ cells. tSNEs analysis of scRNA-seq. KO-specific clusters were labeled as red. n = 3.

(C) Quantification of cell frequencies of different populations in *cKO* Lin$^-$cKit$^+$ cells compared to *Mettl3 f/f* base on scRNA-seq.

(D) Specific clusters in *Mettl3 cKO* are HSC-like. Maximum likelihood of the KO-specific cells into the WT expression models was performed base on the transcriptome profile from scRNA-seq.

(E) Heatmap of differentially expressed genes between HSC cluster and KO SP clusters from scRNA-seq.

(F) Pseudo-time reconstruction of the hierarchy of cell differentiation by Monocle analysis base on scRNA-seq. Left branch indicated HSC commitment to MPPs. Right branch indicated trajectory from HSC to *Mettl3 cKO* specific clusters. n represents number of mice.

with the modest hematopoietic defect observed in *Mettl3* heterozygous mice, these results highlight a wide therapeutic window to target METTL3 in AML.

Single-Cell Profiling Identifies Additional Cell Populations in *Mettl3* cKO Mice

To decipher the effect of *Mettl3* deletion on lineage commitment, identity, and priming of the hematopoietic hierarchy, we performed single-cell RNA-seq (scRNA-seq) using 6000 sorted LK cells (lineage$^-$/cKit$^+$ cells) from three independent control *Mettl3 f/f* and *Mettl3 cKO* mice (Figures S4A–S4C), at 3 weeks post-deletion. Single-cell t-Distributed Stochastic Neighbor Embedding (tSNE) analysis of *Mettl3 f/f* LK cells revealed the expected stem and progenitor clusters, including HSC, MPP, and erythroid, myeloid, and lymphoid progenitors, described previously in scRNA-seq studies (Giladi et al., 2018; Jaitin et al., 2014; Paul et al., 2015) (Figures 4A and S4D; Table S1). However, in *Mettl3 cKO*, the frequencies of basophils (Ba), megakaryocyte-erythroid progenitors (MEPs), megakaryocyte primed populations, and HSC clusters were significantly reduced (Figures 4A–4C). These data suggest that the reduction in myeloid and erythroid mature lineages is already manifested in lineage primed progenitors.

Importantly, projection of distinct cell types by tSNE revealed two populations in the *Mettl3 cKO* samples that were not present in control samples. The two *Mettl3 cKO*-specific populations (KOsp1 and KOsp2) accounted for nearly 30% of all immature LK cells in *Mettl3 cKO* bone marrow (Figures 4A–4C). To interrogate the identity of these *cKO*-specific clusters, we performed a

maximum likelihood projection of KOsp1 and KOsp2 onto the annotated HSPC clusters in control mice. KOsp1 cells predominately clustered with HSCs (50%) and to a lesser degree with MPPs (25%). In contrast, the expression profile of KOsp2 cells was most similar to megakaryocyte progenitors (70%) and had a 20% similarity to HSCs (Figure 4D). A differential expression analysis comparing KOsp1 and KOsp2 cells to WT control HSCs demonstrated a higher expression of cell cycle genes, including *Ki67* and *Cdk1*, and lower expression of key HSC self-renewal regulators and transcription factors, including *Msi2*, *Hoxa9*, *Satb1*, and *Fos* (Figures 4E and S4E). KOsp2 differed from normal megakaryocytic progenitors by their low expression of megakaryocyte lineage-regulating genes, including *Pf4*, *Gp1bb*, *Myb*, and *Gata1*, and increased expression of myeloid and lymphoid genes, including *Cd63*, *Gimap1*, and *Gimap9* (Figure S4F). These gene expression changes are in line with the defects in HSC self-renewal and megakaryocyte maturation that are observed in these cells. These data indicated that the loss of METTL3 resulted in the emergence of actively dividing "HSC like" populations: one (KOsp1) with reduced self-renewal and the other (cKOsp2) acquiring lineage priming toward a megakaryocyte fate.

To better understand the origin of the *cKO*-specific clusters, we performed pseudo-time analysis and hierarchy reconstruction to capture early commitment decisions in HSCs. Both the KOsp clusters and normal MPP clusters were connected to the HSC cluster (Figure 4F). These data suggested that KOsp clusters represent an intermediate state of HSC that branches away from the normal HSC to MPP transition. While many *Mettl3 cKO* HSCs were still capable of normal HSC-to-MPP transition, KOsp1 and KOsp2 ascended from HSCs but the lack of m^6A prevented them from properly committing to normal MPPs. These data strongly suggest that RNA methylation plays a key role in dictating cell identity and lineage commitment in HSCs.

Mettl3 cKO HSCs Lose HSC Identity and Function as MPPs

Since the single-cell sequencing data identified the HSC-like intermediate populations, we next want to delineate the relationship between immunophenotypic HSCs and MPPs and the molecularly defined HSC-like populations. We performed RNA-seq transcriptome profiling of classically defined HSCs and progenitor cells, i.e., HSCs, MPP1s, MPP2s, and MPP4s, whose frequencies were previously found to be altered (Figure S4A). Unsupervised clustering of the differentially expressed genes across all samples distinguished the *Mettl3 cKO* HSPC populations from the controls (by ANOVA test; padj < 0.01) (Figure S5A). The data confirmed that HSPCs from *Mettl3 cKO* mice are distinct from their *Mettl3 f/f* counterparts with a different transcriptome profile. We then examined enrichment of KOsp cluster-specific genes from scRNA-seq with the transcriptional profiles of *Mettl3 f/f* and *Mettl3 cKO* HSCs and MPPs in bulk RNA-seq. Gene set enrichment analysis (GSEA) analysis using the top expressed genes from each spleen (SP) cluster in scRNA-seq (KOsp1/KOsp2 gene sets) revealed that KOsp1 and KOsp2 cells were enriched with *Mettl3 f/f* immunophenotypic HSC signatures rather than MPPs (Figure S5B). Additionally, both KOsp1 and KOsp2 gene sets were enriched in *Mettl3 cKO* HSC cells compared to *Mettl3 cKO* MPPs (Figure S5C). These results indicated that despite the lineage priming features, the scRNA-seq cKO-specific populations still resemble the phenotypic HSCs. It further supports that ablation of m^6A initially alters the cell fate decision of HSCs, and not downstream MPPs.

Next, we further evaluated the altered gene expression program within the HSPC compartment. We performed GSEA of 866 genes that are significantly upregulated in *Mettl3 cKO* HSCs (false discovery rate [FDR] < 0.05), compared with WT HSCs (Table S2). A gene set obtained from the *Mettl3* KO mouse embryonic stem cells (mESCs) (Figures 5A, 5B, and S5D; http://amp.pharm.mssm.edu/Enrichr/) was the top-ranked gene set. These results suggest that loss of METTL3 in HSCs induces a gene expression program that is found in METTL3-deficient naive pluripotent ESCs. Interestingly, this was specific to HSCs, as this analysis in MPPs failed to match with METTL3-deficient ESCs. Thus, the analysis supported that *Mettl3*-deleted HSCs have a lineage priming defect that traps them in a more primitive state. The *Rbm15* KO HSPC signature was also highly enriched in the *Mettl3 cKO* HSC gene expression program (Figures 5B and S5E). RBM15 is an RNA binding protein that recruits the m^6A methyltransferase complex to target mRNAs (Patil et al., 2016). Moreover, the defects observed in *Rbm15* KO mice closely match with many of the phenotypes observed post-METTL3 depletion, suggesting that the phenotypes that have been observed with RBM15 KO mice may be in part attributable to alteration in the m^6A-dependent differentiation program (Patil et al., 2016). These data demonstrate an upregulation of a core m^6A-dependent transcriptional program upon *Mettl3* depletion in HSCs that is shared among models of RNA methylation depletion.

We next performed unbiased GSEA analysis on all 4,733 curated gene sets in the Molecular Signature Database (MSigDB), combined with 92 relevant gene sets from our experimentally derived or published hematopoietic self-renewal and differentiation signatures using HSC and MPP transcriptome profiles from *Mettl3 f/f* and *cKO* mice. We observed a negative enrichment of HSC self-renewal signature and a positive enrichment of ribosome and protein translation gene sets in the *Mettl3 cKO* HSC gene expression profile (Figure 5C). Moreover, protein translation-related ribosome signatures were also enriched in *Mettl3 f/f* MPPs compared to *Mettl3 f/f* HSCs (Figure S5F). We confirmed the increased protein synthesis in *Mettl3 cKO* HSCs based on O-Propargyl-puromycin (OP-Puro) (Figure 5D). These data suggest that there is an alteration in identity in *Mettl3 cKO* HSCs.

As our molecular profiling strongly suggests alterations in cell identity and commitment in METTL3-depleted HSCs, we examined whether these HSCs are functionally defective. To test whether there is an altered identity in *Mettl3 cKO* HSCs, we performed competitive transplantation using sorted HSCs and MPP1s from *Mettl3 f/f* and *cKO* mice (Figure 5E). As observed previously with total bone marrow cells, *Mettl3 cKO* HSCs and MPP1s had low reconstitution within all peripheral cellular compartments (Figure S5G). Within the bone marrow, the control HSCs engrafted normally and chimerism could be measured in all HSPC compartments: HSCs, MPP1s, MPP2s, and MPP4s. The control MPP1s also correctly reconstituted

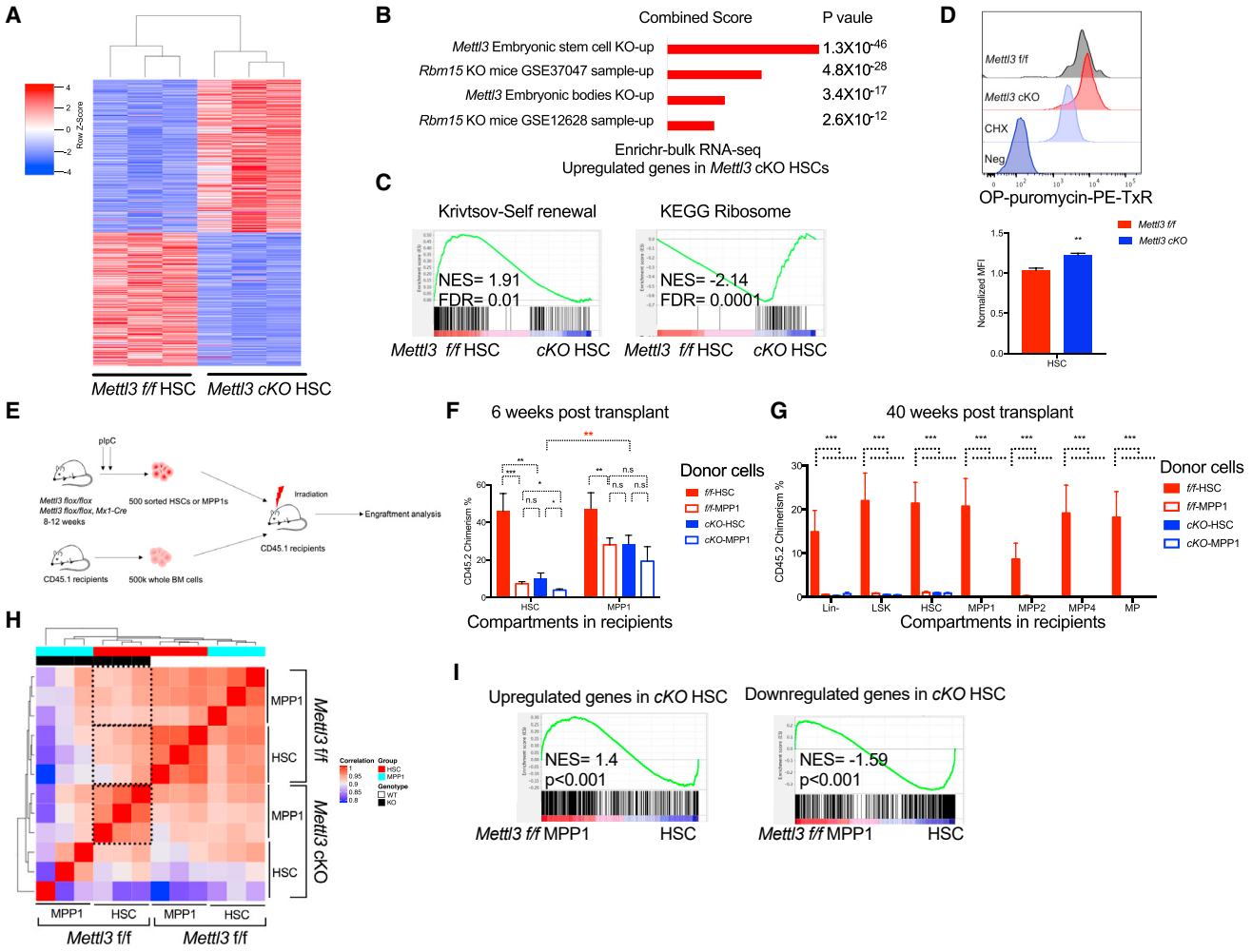

Figure 5. *Mettl3*-Deleted HSCs Are More Functionally and Molecularly MPP-like

(A) Significant differentially expressed genes (padj < 0.05) in *cKO* HSCs compared to *Mettl3 f/f* were shown as heatmap.

(B) Differentially expressed genes in *Mettl3 cKO* HSCs were enriched with *Mettl3* KO ESC and RBM15 KO LSK expression signatures. Enrichr analysis using upregulated genes in METTL3-depleted HSCs from bulk RNA-seq.

(C) Unbiased gene set enrichment analysis using 4,733 curated gene sets against the rank list of differential expressed genes between *Mettl3 f/f* and *cKO* HSCs. Self-renewal signature was negatively enriched in *Mettl3 cKO* HSCs. Translation and ribosome gene sets were positively enriched in *Mettl3 cKO* HSCs.

(D) Increased global translation in *Mettl3 cKO* HSCs. Representative histograms (top) and quantification (bottom) of OP-Puro incorporation into sorted *Mettl3 f/f* and *cKO* HSCs.

(E) Scheme of transplant strategy in (F). Sorted HSCs and MPP1s from *Mettl3 f/f* and *Mettl3 cKO* mice were injected into CD45.1 recipient mice with CD45.1 competitor BM cells.

(F) *Mettl3 cKO* HSCs function as MPP1s in competitive transplant assays. Engraftment of CD45.2 donor cells was analyzed in HSPCs from recipient mice at 6 weeks. n = 10.

(G) Engraftment of CD45.2 donor cells was analyzed in HSPCs from recipient mice at 40 weeks. n = 10.

(H) Spearman correlation among HSC and MPP1 populations from *Mettl3 f/f* and *Mettl3 cKO* mice.

(I) Gene set enrichment analysis of up- or downregulated genes in *Mettl3 cKO* HSC identified by bulk RNA-seq, against the rank list of differentially expressed genes between *Mettl3 f/f* HSC and *Mettl3 f/f* MPP1. Mean and SEM are shown (*p < 0.05, **p < 0.01, ***p < 0.001, and ****p < 0.0001). n represents number of mice.

the MPP1 compartment, thus validating our sorting strategy in this functional assay (Figures 5F and S5H). However, the *Mettl3 cKO* HSCs demonstrated chimerism within the phenotypic MPP1 compartment but not within the HSC compartment (Figure 5F). Additionally, these transplanted HSCs in the MPP compartment behaved as MPP1s, as they were no longer detected at long-term analysis (40 weeks post-transplant) (Figures 5G and S5I). This altered fate was also validated by Spearman correlation analysis using gene expression profiles of *Mettl3 f/f* and *Mettl3 cKO* HSCs and MPP1s. Gene expressions between *cKO* HSCs and control HSCs were less correlated, and the *cKO* HSCs' gene profile correlated similarly to control HSCs or MPP1s (Figure 5H). Furthermore, GSEA analysis also showed that *Mettl3 cKO* HSCs were indeed enriched for *Mettl3 f/f*

MPP1 and MPP2 gene expression signatures (Figures 5I and S5J). These data indicated that m^{6}A-ablated HSCs are more molecularly and functionally similar to MPP1 cells.

m^{6}A Regulates HSC Asymmetric and Symmetric Division by Modulating *Myc* mRNA

We next sought to understand the molecular basis for abnormal cell fate decision and differentiation upon loss of m^{6}A in HSCs. Given that m^{6}A ablation traps HSCs in a more primitive state during HSC-to-MPP transition, we hypothesized that genes essential for this transition would differentially increase their m^{6}A abundance in MPPs compared to HSCs. Thus, we reanalyzed previously obtained m^{6}A profiles in HSCs and MPPs and selected genes with higher m^{6}A marks in MPPs (Li et al., 2018). To identify m^{6}A and METTL3 direct targets, we then intersected the list of increased m^{6}A methylated mRNAs in MPPs with the differentially expressed genes in HSCs upon *Mettl3* deletion, resulting in eight genes (Figures 6A and S6A; Table S3). MYC was among these genes known to be a critical target of mRNA methylation (Vu et al., 2017a). Moreover, *Mettl3* deletion partially phenocopied the expanded HSPC compartment found in the *Myc*-deficient mice (Bahr et al., 2018; Wilson et al., 2004). To further determine if MYC is a direct functional target of m^{6}A in HSCs, we performed methylated RNA immunoprecipitation (MeRIP)-qPCR and found reduced enrichment of m^{6}A in *Myc* transcripts in *Mettl3 cKO* HSPCs (Figure 6B). Overall, these data suggest that *Myc* could be a functional downstream target of m^{6}A and METTL3 in HSCs.

To directly assess HSC fate commitment and to evaluate MYC expression after *Mettl3* deletion, we performed paired daughter cell division assays based on intracellular staining of NUMB and MYC proteins. Previous studies showed that HSCs can undergo three fate choices: symmetric renewal, symmetric commitment, and asymmetric cell division. Cellular commitment toward a differentiation cell fate is measured by increased NUMB staining in the post-dividing HSCs (Kharas et al., 2010; Park et al., 2014; Wu et al., 2007). *Mettl3* deletion results in a significant reduction in symmetric commitment (25% to 7%; multiple t test; $p = 0.000287$) with an increase in symmetric renewal division and no effect on asymmetric cell division (Figures 6C and 6D). Surprisingly, we observed that MYC can be segregated in the dividing HSCs asymmetrically, symmetrically "low," and symmetrically "high" in a manner correlated closely with the pattern of NUMB (Figures 6D and 6E). This indicated that MYC abundance could also be used as a marker for cellular commitment (Kharas et al., 2010; Park et al., 2014; Wu et al., 2007). As observed in NUMB staining, we found fewer daughter cells with high MYC staining (20% to 7%; multiple t test; $p = 0.0307$) (Figure 6D). These data suggest that METTL3 controlled the abundance of MYC in HSCs at a decision point that dictates the choice between symmetric self-renewal versus symmetric commitment.

To determine if asymmetric segregation of MYC was already determined at the level of mRNA, we performed fluorescence *in situ* hybridization (FISH) of *Myc* mRNA and fluorescence immunostaining of NUMB. Interestingly, *Myc* mRNA also can be segregated to daughter cells asymmetrically, symmetrically "low," and symmetrically "high" in a manner correlating to NUMB and MYC (Figure 6F). Furthermore, consistent with our scRNA-seq and RNA-seq results, the *Myc* mRNA was dramatically reduced in *Mettl3 cKO* HSCs (Figures 6G and 6H). These data suggest that m^{6}A RNA methylation controls *Myc* mRNA abundance that is required for HSC commitment. Given that m^{6}A modification affects mRNA stability, we hypothesized that the reduced *Myc* mRNA level in *Mettl3 cKO* HSCs is due to decreased *Myc* mRNA stability. Indeed, the half-time of *Myc* mRNA was significantly decreased in *Mettl3 cKO* HSCs (Figures 6I and S6B). Reintroduction of MYC in *Mettl3 cKO* HSCs partially rescued the HSC commitment defect (Figure S6C and S6D). Overall, these data suggest that m^{6}A controls HSC symmetric commitment through MYC regulation.

Next, to determine whether the failure of HSCs to properly differentiate is functionally driven by reduced MYC abundance during cell division, we overexpressed MYC in sorted *Mettl3 cKO* LSK cells and performed competitive bone marrow transplants. MYC overexpression resulted in a rescue in the peripheral blood and bone marrow HSPC compartment chimerism in mice transplanted with *Mettl3 cKO* HSPCs (Figures 7A–7C, S7A, and S7B). Furthermore, this increased chimerism could be observed within the HSC compartments in 5 out of the 10 mice (Figure S7B). A lethal myeloproliferative and AML-like disease was observed in the MYC overexpression group as previously reported (Figure S7C) (Luo et al., 2005), suggesting that highly expressed MYC could bypass the requirement for METTL3 in myeloid leukemia. These *in vitro* and *in vivo* data suggest that restoring MYC can at least partially override defects in HSC commitment and drive normal HSC differentiation.

Altogether, these data suggest that MYC mRNA and protein is a marker for commitment and m^{6}A-deficient HSCs are partially blocked in their ability to differentiate.

METTL3 Catalytic Function Controls MYC Abundance and HSC Commitment *In Vivo*

As METTL3 may have additional functions beyond its methyltransferase activity, we then assessed if METTL3's catalytic function is directly responsible for alterations in MYC abundance and HSC commitment. To this end, we overexpressed METTL3 or a catalytically dead METTL3 mutant (METTL3-CD) and found that it rescued the reduced overall MYC abundance in either *Mettl3*-siRNA transfected HSCs or in *cKO* HSCs (Figures 7D and S7D). Additionally, overexpression of METTL3, but not METTL3-CD, partially rescued HSC symmetric commitment in the paired daughter cell division assay and *Mettl3 cKO* HSC engraftment (Figures 7E, 7F, and S7E). Moreover, METTL3, but not METTL3-CD, significantly enhanced normal HSPC reconstitution capacity *in vivo*, suggesting that increased methyltransferase activity can enhance HSPC engraftment (Figure S7F). Overall, these data suggest that METTL3 catalytic activity is essential for MYC regulation, HSC commitment, and HSC function.

DISCUSSION

Here, by integrating transcriptome profiling with single-cell RNA sequencing and single-cell assays, we show that m^{6}A is required for the early cell fate decision in adult HSCs. Our studies find that

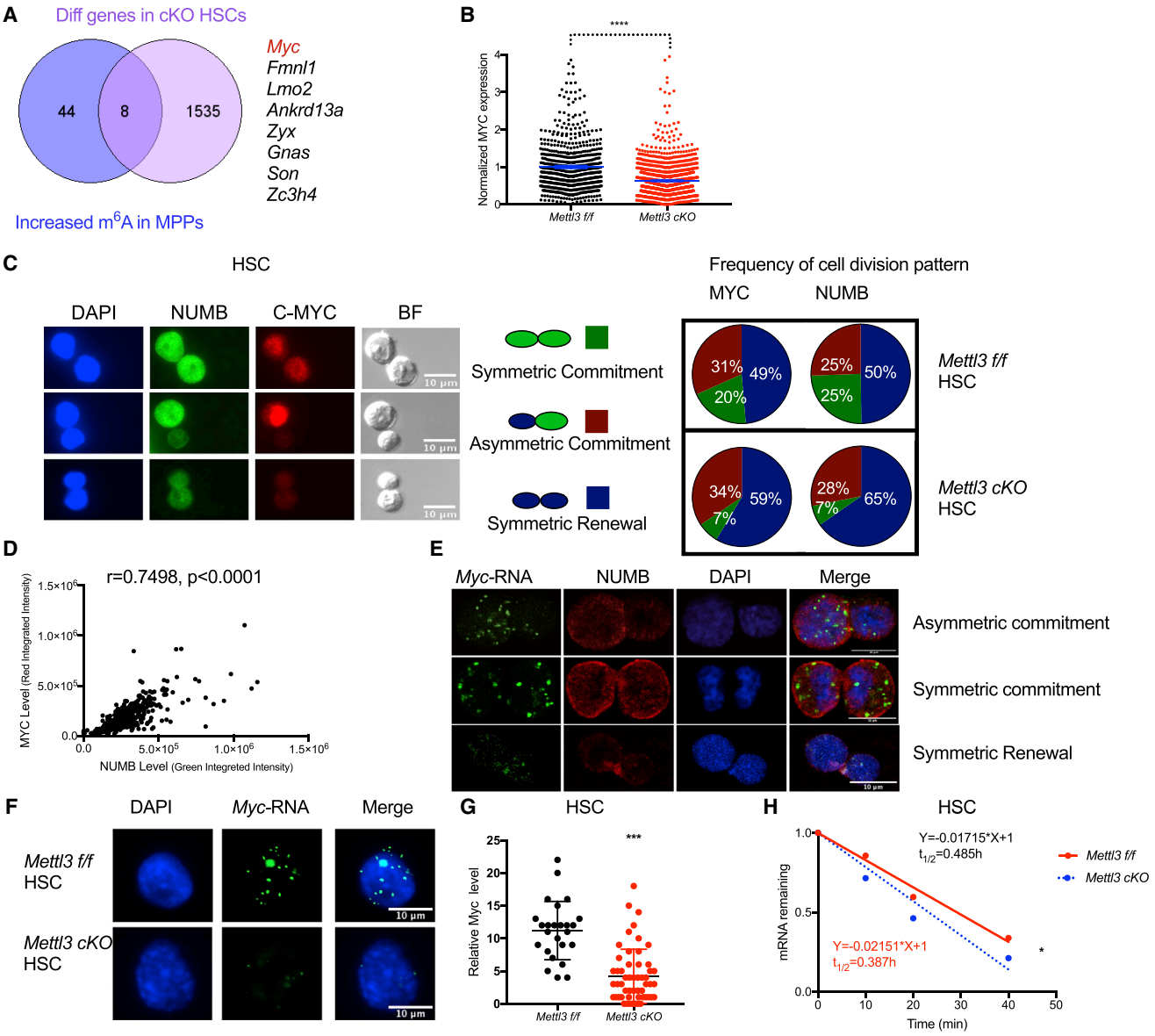

Figure 6. *Mettl3* Is Required for HSC Symmetric Commitment by Regulating mRNA Stability of *Myc*

(A) Overlap of the 52 genes that have increased m^{6}A abundance in MPPs than HSCs with differentially expressed genes between *Mettl3 f/f* and *cKO* HSCs, as depicted in a Venn diagram. *Myc* is highlighted in red.

(B) m^{6}A enrichment in the *Myc* transcript in *Mettl3 f/f* and *cKO* HSPCs was assessed by MeRIP-qPCR. Two primers were used to indicate different m^{6}A sites on *Myc* RNA.

(C) MYC protein level is reduced in *Mettl3 cKO* HSCs upon cell division. MYC expression in *Mettl3 cKO* HSCs compared to *Mettl3 f/f* HSCs as quantified by immunofluorescence.

(D) *Mettl3 cKO* HSCs fail to undergo symmetric commitment compared to control HSCs. Left: representative immunofluorescence images of paired daughter cells stained with DAPI (blue), NUMB (green), MYC (red), and brightfield. Right: percentages of doublet cells in each type of cell division. Number of daughter pairs assessed**:** *Mettl3 f/f* n = 223; *cKO* n = 245. n represents number of paired HSCs measured.

(E) MYC expression correlates with NUMB expression during HSC division.

(F) *Myc* mRNA can be segregated into daughter cells asymmetrically, symmetrically high, and symmetrically low. Representative images of fluorescence *in situ* hybridization (FISH) of *Myc* mRNA (green) and fluorescence immunostaining of NUMB (red) and DAPI (blue) in HSCs.

(G) *Myc* mRNA is significantly decreased in *Mettl3 cKO* HSCs. Representative images of FISH of *Myc* mRNA (green) and DAPI (blue) in *Mettl3 f/f* and *Mettl3 cKO* HSCs.

(H) Quantification of *Myc* mRNA in HSCs from *Mettl3 f/f* and *Mettl3 cKO* mice.

(I) The mRNA half-life (t1/2) of *Myc* transcripts in *Mettl3 f/f* and *Mettl3 cKO* HSCs. Mean and SEM are shown (*p < 0.05, **p < 0.01, ***p < 0.001, and ****p < 0.0001).

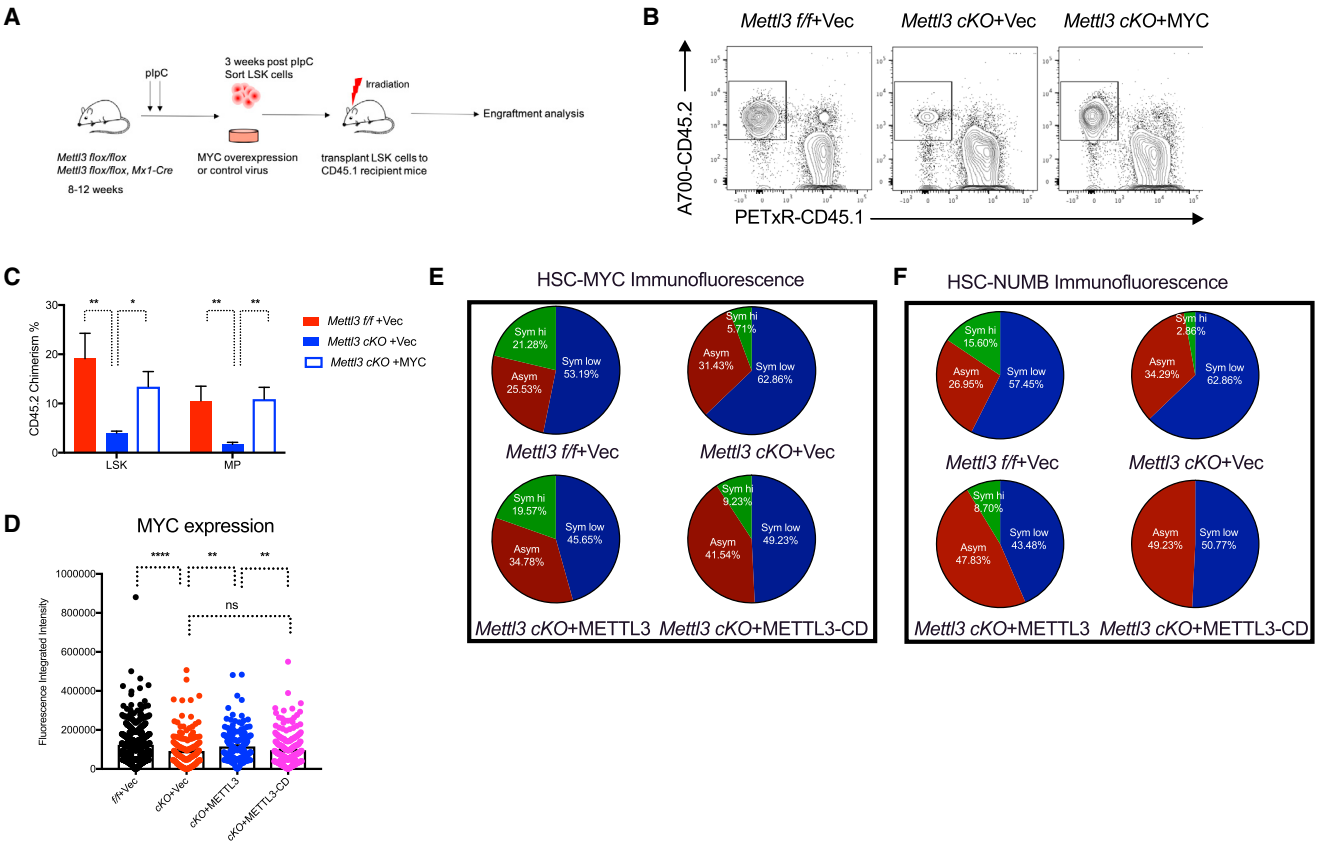

Figure 7. MYC Overexpression Can Partially Rescue Reconstitution Defect in *Mettl3 cKO* HSPCs

(A) Scheme of experiment strategy. LSK cells were sorted from *Mettl3 f/f* and *Mettl3 cKO* mice and transduced with control and MYC overexpression retrovirus. Donor cells were then transplanted into CD45.1 recipient mice with CD45.1 competitor BM cells.

(B) Quantification of the frequency of donor-derived cells was shown in LSK and MP populations, n = 9. n represents number of mice.

(C) MYC overexpression rescues the repopulating defect of *Mettl3 cKO* LSKs. Representative flow cytometry plots of engraftment of donor-derived CD45.2 cells.

(D) METTL3 overexpression rescue MYC expression defect in *Mettl3 cKO* HSCs as quantified by immunofluorescence.

(E and F) Paired daughter cell assay using sorted HSCs from *Mettl3 f/f* and *Mettl3 cKO* mice transfected with vectors expressing METTL3 or METTL3-CD or empty vector as control to indicate MYC (E) and NUMB (F) expression. Pie chart shows different types of cell divisions in HSCs as indicated. Number of daughter pairs assessed: *Mettl3 f/f* +Vec, n = 141; *cKO*+Vec, n = 35; *cKO*+METTL3 WT, n = 45; and *cKO*+METTL3 CD, n = 65. n represents number of paired HSCs measured. Mean and SEM are shown (*p < 0.05, **p < 0.01, ***p < 0.001, and ****p < 0.0001).

m^{6}A controls HSC identity by affecting the symmetric commitment step, while asymmetric divisions are less affected. m^{6}A is a known regulator of *Myc* expression in HSCs. We show that *Myc* functions to promote HSC symmetric commitment, and its loss in m^{6}A-deficient cells results in the formation of a cell type with MPP-like identity, rather than an accumulation in the HSC population, as is currently thought in the field (Lee et al., 2019; Yao et al., 2018). The current thinking about m^{6}A in normal hematopoiesis is that m^{6}A controls HSC differentiation without affecting self-renewal or proliferation. Here, we show that the accumulated immunophenotypic "HSCs" that were identified in previous studies are instead a blocked HSC-MPP-like cell population. These cells behave as MPP-like cells as they exhaust and thus have reduced self-renewal *in vivo*. These HSC-like intermediate cells are also metabolically active and highly proliferative, but they fail to symmetrically commit and differentiate. Our study shows that m^{6}A controls cell identity by regulating the symmetric commitment of HSCs during division at the early cell fate determination point. These intermediate populations could also be used to further understand the relationship between HSC expansion and commitment toward MPPs.

Interestingly, while m^{6}A reader YTHDF2-deficient mice also exhibited increased HSCs number, *Ythdf2* knockout HSCs demonstrated improved functional and regenerative capacity in contrast to what we observed in *Mettl3*-deficient HSCs (Li et al., 2018). These data suggest that YTHDF2 depletion may promote HSC self-renewal without compromising commitment, resulting in functional HSC expansion.

MYC was reported as a target of m^{6}A in regulating myeloid leukemia and HSCs (Lee et al., 2019; Vu et al., 2017a). However, it is unclear how m^{6}A controls MYC and in which step MYC affects HSCs. We identified MYC as a functional target of m^{6}A that facilitates the transition from HSCs to MPPs during the early steps of cell fate determination and its RNA stability is controlled by m^{6}A. Surprisingly, we demonstrated that MYC mRNA and protein could be segregated either asymmetrically or symmetrically

during HSC division. An asymmetric partition of MYC was observed during T cell activation (Pollizzi et al., 2016; Verbist et al., 2016). Thus, the insight of m^{6}A in controlling symmetric commitment by modulating MYC could be a general mechanism for m^{6}A regulation of cell fate. Several known m^{6}A-dependent cell fate regulations are consistent with our model. For example, in mouse ESCs and in naive T cells, loss of m^{6}A locks the cells in its naive state and prevents differentiation (Geula et al., 2015; Li et al., 2017).

We previously reported that depletion of METTL3 in human AML cells results in increased *MYC* mRNA abundance and reduced translational efficiency, which finally leads to decreased MYC protein (Vu et al., 2017a). In contrast, METTL3 depletion in normal murine HSCs results in a decrease in *Myc* mRNA and protein levels, suggesting a cellular-context-dependent regulation of m^{6}A targets or differential effects after transient versus prolonged depletion of m^{6}A.

Previous studies revealed that m^{6}A is required for leukemogenesis and AML cell survival, prompting the search for inhibitors to block this pathway as a potential therapeutic strategy in myeloid malignancies and cancer (Barbieri et al., 2017; Vu et al., 2017a; Weng et al., 2018). Our work describes the consequences of METTL3 depletion in the blood system and indicates the importance of this pathway in normal hematopoietic development at various stages including in more mature lineages. Importantly, our data also demonstrate that transient siRNA depletion of METTL3 results in reversible and modest effects on hematopoiesis. However, the true therapeutic window for METTL3 inhibitors will only be known once potent and selective inhibitors are developed.

Overall, our findings demonstrate that m^{6}A is essential for the maintenance of HSC identity and symmetric commitment. As the control of symmetric commitment in adult stem cells is critical for rapidly replenishing tissue compartments after stress or damage, our study highlights the role of RNA methylation in adult stem cell commitment and fate determination.

STAR★METHODS

Detailed methods are provided in the online version of this paper and include the following:

- KEY RESOURCES TABLE
- LEAD CONTACT AND MATERIALS AVAILABILITY
- EXPERIMENTAL MODEL AND SUBJECT DETAILS
  - Mice
- METHOD DETAILS
  - Noncompetitive Transplant
  - PCR and Quantitative RT-PCR
  - Flow Cytometry and Cell Sorting
  - Peripheral Blood Analysis
  - Western-Blot
  - Determination of Relative m^{6}A Levels
  - Colony Assay
  - Competitive Transplant
  - HSPC Cell Sorting, Cell Culture, Retroviral Infection, and Transplant
  - O-Propargyl-puromycin (OP-Puro) Flow Analysis
  - Immunofluorescence
  - RNA-FISH in Conjugation with Fluorescent Immunostaining
  - RNA Stability Assay
  - Electroporation Transfection
  - m^{6}A-seq Peak Enrichment Analysis
  - MeRIP-qPCR
  - RNA-Seq
  - Single-Cell RNA-Seq
- QUANTIFICATION AND STATISTICAL ANALYSIS
- DATA AND CODE AVAILABILITY

SUPPLEMENTAL INFORMATION

Supplemental Information can be found online at https://doi.org/10.1016/j.celrep.2019.07.032.

ACKNOWLEDGMENTS

We would like to thank members of the Kharas, Jaffrey, and Landau laboratories and colleagues for helpful advice and suggestions. We thank Dr. Linheng Li for providing the m^{6}A-seq information in LT/ST HSCs and MPPs. We thank Brooke Greenstein from Basepair for bioinformatics analysis. We would like to thank the Weill Cornell Medicine Epigenomics Core for their assistance with single-cell RNA sequencing. We thank the Integrated Genomics Operation (IGO) core in MSKCC for their help with our bulk RNA sequencing. M.G.K. is a Scholar of the Leukemia and Lymphoma Society and supported by the US NIH National Institute of Diabetes Digestive and Kidney Diseases Career Development Award; NIDDK NIH R01-DK101989-01A1; NCI 1R01CA193842-01, R01HL135564, and R01CA225231-01; the Kimmel Scholar Award; the V-Scholar Award; the Geoffrey Beene Award; the Starr Cancer Consortium; the Alex's Lemonade Stand A Award; the LLS Translation Research Program; the Susan and Peter Solomon Fund; and the Tri-Institutional Stem Cell Initiative 2016-014. D.A.L. is supported by the Burroughs Wellcome Fund Career Award for Medical Scientists; the ASH Scholar Award; Pershing Square Sohn Prize for Young Investigators in Cancer Research, the NIH Director's New Innovator Award (DP2-CA239065); the National Heart, Lung, and Blood Institute (R01HL145283-01); a Stand Up to Cancer Innovative Research Grant (SU2C-AACR-IRG-0616); and the Leukemia Lymphoma Society Translational Research Program. S.R.J. is supported by R01CA186702. H.L. is supported by NYSTEM training award contract C32599GG. B.F.P. is supported by F32CA22104. L.P.V. is supported by K99 CA229993 and the LLS Career Development Award. This work was also supported by P30CA008748.

AUTHOR CONTRIBUTIONS

Y.C. led this project, designed and performed experiments, analyzed data, and wrote the manuscript. H.L. designed and performed experiments, analyzed data, and wrote the manuscript. F.I. analyzed the single-cell RNA-seq data and edited the manuscript. B.F.P. performed the global m^{6}A assay, analyzed m^{6}A-seq, and edited the manuscript. A.S. and S.G. provided experimental supports. L.P.V. provided help with the experimental design and wrote the manuscript. S.R.J. and D.A.L. supervised the project and edited the manuscript. M.G.K. directed the project, analyzed data, and wrote the manuscript.

DECLARATION OF INTERESTS

D.A.L. received consulting honoraria from Pharmacyclics. S.R.J. is a scientific founder of Gotham Therapeutics and has equity in this company.

Received: February 6, 2019
Revised: May 17, 2019
Accepted: July 11, 2019
Published: August 13, 2019

REFERENCES

Attar, E.C., and Scadden, D.T. (2004). Regulation of hematopoietic stem cell growth. Leukemia *18*, 1760–1768.

Bahr, C., von Paleske, L., Uslu, V.V., Remeseiro, S., Takayama, N., Ng, S.W., Murison, A., Langenfeld, K., Petretich, M., Scognamiglio, R., et al. (2018). A Myc enhancer cluster regulates normal and leukaemic haematopoietic stem cell hierarchies. Nature *553*, 515–520.

Barbieri, I., Tzelepis, K., Pandolfini, L., Shi, J., Millán-Zambrano, G., Robson, S.C., Aspris, D., Migliori, V., Bannister, A.J., Han, N., et al. (2017). Promoter-bound METTL3 maintains myeloid leukaemia by m^6A-dependent translation control. Nature *552*, 126–131.

Batista, P.J., Molinie, B., Wang, J., Qu, K., Zhang, J., Li, L., Bouley, D.M., Lujan, E., Haddad, B., Daneshvar, K., et al. (2014). m(6)A RNA modification controls cell fate transition in mammalian embryonic stem cells. Cell Stem Cell *15*, 707–719.

Boriack-Sjodin, P.A., Ribich, S., and Copeland, R.A. (2018). RNA-modifying proteins as anticancer drug targets. Nat. Rev. Drug Discov. *17*, 435–453.

Butler, A., Hoffman, P., Smibert, P., Papalexi, E., and Satija, R. (2018). Integrating single-cell transcriptomic data across different conditions, technologies, and species. Nat. Biotechnol. *36*, 411–420.

Cheng, T., Rodrigues, N., Shen, H., Yang, Y., Dombkowski, D., Sykes, M., and Scadden, D.T. (2000). Hematopoietic stem cell quiescence maintained by p21cip1/waf1. Science *287*, 1804–1808.

Coots, R.A., Liu, X.M., Mao, Y., Dong, L., Zhou, J., Wan, J., Zhang, X., and Qian, S.B. (2017). m(6)A Facilitates eIF4F-Independent mRNA Translation. Mol. Cell *68*, 504–514.e7.

Geula, S., Moshitch-Moshkovitz, S., Dominissini, D., Mansour, A.A., Kol, N., Salmon-Divon, M., Hershkovitz, V., Peer, E., Mor, N., Manor, Y.S., et al. (2015). Stem cells. m6A mRNA methylation facilitates resolution of naïve pluripotency toward differentiation. Science *347*, 1002–1006.

Giladi, A., Paul, F., Herzog, Y., Lubling, Y., Weiner, A., Yofe, I., Jaitin, D., Cabezas-Wallscheid, N., Dress, R., Ginhoux, F., et al. (2018). Single-cell characterization of haematopoietic progenitors and their trajectories in homeostasis and perturbed haematopoiesis. Nat. Cell Biol. *20*, 836–846.

Gundry, M.C., Brunetti, L., Lin, A., Mayle, A.E., Kitano, A., Wagner, D., Hsu, J.I., Hoegenauer, K.A., Rooney, C.M., Goodell, M.A., and Nakada, D. (2016). Highly Efficient Genome Editing of Murine and Human Hematopoietic Progenitor Cells by CRISPR/Cas9. Cell Rep. *17*, 1453–1461.

Hock, H., Hamblen, M.J., Rooke, H.M., Schindler, J.W., Saleque, S., Fujiwara, Y., and Orkin, S.H. (2004). Gfi-1 restricts proliferation and preserves functional integrity of haematopoietic stem cells. Nature *431*, 1002–1007.

Jaitin, D.A., Kenigsberg, E., Keren-Shaul, H., Elefant, N., Paul, F., Zaretsky, I., Mildner, A., Cohen, N., Jung, S., Tanay, A., and Amit, I. (2014). Massively parallel single-cell RNA-seq for marker-free decomposition of tissues into cell types. Science *343*, 776–779.

Kharas, M.G., Lengner, C.J., Al-Shahrour, F., Bullinger, L., Ball, B., Zaidi, S., Morgan, K., Tam, W., Paktinat, M., Okabe, R., et al. (2010). Musashi-2 regulates normal hematopoiesis and promotes aggressive myeloid leukemia. Nat. Med. *16*, 903–908.

Kiel, M.J., Yilmaz, O.H., Iwashita, T., Yilmaz, O.H., Terhorst, C., and Morrison, S.J. (2005). SLAM family receptors distinguish hematopoietic stem and progenitor cells and reveal endothelial niches for stem cells. Cell *121*, 1109–1121.

Knoblich, J.A. (2008). Mechanisms of asymmetric stem cell division. Cell *132*, 583–597.

Lee, H., Bao, S., Qian, Y., Geula, S., Leslie, J., Zhang, C., Hanna, J.H., and Ding, L. (2019). Stage-specific requirement for Mettl3-dependent m(6)A mRNA methylation during haematopoietic stem cell differentiation. Nat. Cell Biol. *21*, 700–709.

Li, H.B., Tong, J., Zhu, S., Batista, P.J., Duffy, E.E., Zhao, J., Bailis, W., Cao, G., Kroehling, L., Chen, Y., et al. (2017). m^6A mRNA methylation controls T cell homeostasis by targeting the IL-7/STAT5/SOCS pathways. Nature *548*, 338–342.

Li, Z., Qian, P., Shao, W., Shi, H., He, X.C., Gogol, M., Yu, Z., Wang, Y., Qi, M., Zhu, Y., et al. (2018). Suppression of m(6)A reader Ythdf2 promotes hematopoietic stem cell expansion. Cell Res. *28*, 904–917.

Liu, F., Cheng, G., Hamard, P.J., Greenblatt, S., Wang, L., Man, N., Perna, F., Xu, H., Tadi, M., Luciani, L., and Nimer, S.D. (2015). Arginine methyltransferase PRMT5 is essential for sustaining normal adult hematopoiesis. J. Clin. Invest. *125*, 3532–3544.

Luo, H., Li, Q., O'Neal, J., Kreisel, F., Le Beau, M.M., and Tomasson, M.H. (2005). c-Myc rapidly induces acute myeloid leukemia in mice without evidence of lymphoma-associated antiapoptotic mutations. Blood *106*, 2452–2461.

Lv, J., Zhang, Y., Gao, S., Zhang, C., Chen, Y., Li, W., Yang, Y.G., Zhou, Q., and Liu, F. (2018). Endothelial-specific m^6A modulates mouse hematopoietic stem and progenitor cell development via Notch signaling. Cell Res. *28*, 249–252.

Mauer, J., Luo, X., Blanjoie, A., Jiao, X., Grozhik, A.V., Patil, D.P., Linder, B., Pickering, B.F., Vasseur, J.J., Chen, Q., et al. (2017). Reversible methylation of m^6A_m in the 5′ cap controls mRNA stability. Nature *541*, 371–375.

Meyer, K.D., and Jaffrey, S.R. (2017). Rethinking m^6A Readers, Writers, and Erasers. Annu. Rev. Cell Dev. Biol. *33*, 319–342.

Meyer, K.D., Patil, D.P., Zhou, J., Zinoviev, A., Skabkin, M.A., Elemento, O., Pestova, T.V., Qian, S.B., and Jaffrey, S.R. (2015). 5′ UTR m(6)A Promotes Cap-Independent Translation. Cell *163*, 999–1010.

Morrison, S.J., and Kimble, J. (2006). Asymmetric and symmetric stem-cell divisions in development and cancer. Nature *441*, 1068–1074.

Oguro, H., Ding, L., and Morrison, S.J. (2013). SLAM family markers resolve functionally distinct subpopulations of hematopoietic stem cells and multipotent progenitors. Cell Stem Cell *13*, 102–116.

Park, S.M., Deering, R.P., Lu, Y., Tivnan, P., Lianoglou, S., Al-Shahrour, F., Ebert, B.L., Hacohen, N., Leslie, C., Daley, G.Q., et al. (2014). Musashi-2 controls cell fate, lineage bias, and TGF-β signaling in HSCs. J. Exp. Med. *211*, 71–87.

Patil, D.P., Chen, C.K., Pickering, B.F., Chow, A., Jackson, C., Guttman, M., and Jaffrey, S.R. (2016). m(6)A RNA methylation promotes XIST-mediated transcriptional repression. Nature *537*, 369–373.

Paul, F., Arkin, Y., Giladi, A., Jaitin, D.A., Kenigsberg, E., Keren-Shaul, H., Winter, D., Lara-Astiaso, D., Gury, M., Weiner, A., et al. (2015). Transcriptional Heterogeneity and Lineage Commitment in Myeloid Progenitors. Cell *163*, 1663–1677.

Ping, X.L., Sun, B.F., Wang, L., Xiao, W., Yang, X., Wang, W.J., Adhikari, S., Shi, Y., Lv, Y., Chen, Y.S., et al. (2014). Mammalian WTAP is a regulatory subunit of the RNA N6-methyladenosine methyltransferase. Cell Res. *24*, 177–189.

Pollizzi, K.N., Sun, I.H., Patel, C.H., Lo, Y.C., Oh, M.H., Waickman, A.T., Tam, A.J., Blosser, R.L., Wen, J., Delgoffe, G.M., and Powell, J.D. (2016). Asymmetric inheritance of mTORC1 kinase activity during division dictates CD8(+) T cell differentiation. Nat. Immunol. *17*, 704–711.

Rodriguez-Fraticelli, A.E., Wolock, S.L., Weinreb, C.S., Panero, R., Patel, S.H., Jankovic, M., Sun, J., Calogero, R.A., Klein, A.M., and Camargo, F.D. (2018). Clonal analysis of lineage fate in native haematopoiesis. Nature *553*, 212–216.

Roundtree, I.A., Evans, M.E., Pan, T., and He, C. (2017). Dynamic RNA Modifications in Gene Expression Regulation. Cell *169*, 1187–1200.

Schwartz, S., Mumbach, M.R., Jovanovic, M., Wang, T., Maciag, K., Bushkin, G.G., Mertins, P., Ter-Ovanesyan, D., Habib, N., Cacchiarelli, D., et al. (2014). Perturbation of m6A writers reveals two distinct classes of mRNA methylation at internal and 5′ sites. Cell Rep. *8*, 284–296.

Slobodin, B., Han, R., Calderone, V., Vrielink, J., Loayza-Puch, F., Elkon, R., and Agami, R. (2017). Transcription Impacts the Efficiency of mRNA Translation via Co-transcriptional N6-adenosine Methylation. Cell *169*, 326–337.e12.

Trapnell, C., Cacchiarelli, D., Grimsby, J., Pokharel, P., Li, S., Morse, M., Lennon, N.J., Livak, K.J., Mikkelsen, T.S., and Rinn, J.L. (2014). The dynamics and regulators of cell fate decisions are revealed by pseudotemporal ordering of single cells. Nat. Biotechnol. *32*, 381–386.

Verbist, K.C., Guy, C.S., Milasta, S., Liedmann, S., Kamiński, M.M., Wang, R., and Green, D.R. (2016). Metabolic maintenance of cell asymmetry following division in activated T lymphocytes. Nature *532*, 389–393.

Vu, L.P., Pickering, B.F., Cheng, Y., Zaccara, S., Nguyen, D., Minuesa, G., Chou, T., Chow, A., Saletore, Y., MacKay, M., et al. (2017a). The N^6-methyladenosine (m^6A)-forming enzyme METTL3 controls myeloid differentiation of normal hematopoietic and leukemia cells. Nat. Med. *23*, 1369–1376.

Vu, L.P., Prieto, C., Amin, E.M., Chhangawala, S., Krivtsov, A., Calvo-Vidal, M.N., Chou, T., Chow, A., Minuesa, G., Park, S.M., et al. (2017b). Functional screen of MSI2 interactors identifies an essential role for SYNCRIP in myeloid leukemia stem cells. Nat. Genet. *49*, 866–875.

Wang, X., Zhao, B.S., Roundtree, I.A., Lu, Z., Han, D., Ma, H., Weng, X., Chen, K., Shi, H., and He, C. (2015). N(6)-methyladenosine Modulates Messenger RNA Translation Efficiency. Cell *161*, 1388–1399.

Weng, H., Huang, H., Wu, H., Qin, X., Zhao, B.S., Dong, L., Shi, H., Skibbe, J., Shen, C., Hu, C., et al. (2018). METTL14 Inhibits Hematopoietic Stem/Progenitor Differentiation and Promotes Leukemogenesis via mRNA m(6)A Modification. Cell Stem Cell *22*, 191–205.e9.

Wilson, A., Murphy, M.J., Oskarsson, T., Kaloulis, K., Bettess, M.D., Oser, G.M., Pasche, A.C., Knabenhans, C., Macdonald, H.R., and Trumpp, A. (2004). c-Myc controls the balance between hematopoietic stem cell self-renewal and differentiation. Genes Dev. *18*, 2747–2763.

Wu, M., Kwon, H.Y., Rattis, F., Blum, J., Zhao, C., Ashkenazi, R., Jackson, T.L., Gaiano, N., Oliver, T., and Reya, T. (2007). Imaging hematopoietic precursor division in real time. Cell Stem Cell *1*, 541–554.

Xiao, W., Adhikari, S., Dahal, U., Chen, Y.S., Hao, Y.J., Sun, B.F., Sun, H.Y., Li, A., Ping, X.L., Lai, W.Y., et al. (2016). Nuclear m(6)A Reader YTHDC1 Regulates mRNA Splicing. Mol. Cell *61*, 507–519.

Yao, Q.J., Sang, L., Lin, M., Yin, X., Dong, W., Gong, Y., and Zhou, B.O. (2018). Mettl3-Mettl14 methyltransferase complex regulates the quiescence of adult hematopoietic stem cells. Cell Res. *28*, 952–954.

Zhang, C., Chen, Y., Sun, B., Wang, L., Yang, Y., Ma, D., Lv, J., Heng, J., Ding, Y., Xue, Y., et al. (2017). m^6A modulates haematopoietic stem and progenitor cell specification. Nature *549*, 273–276.

STAR★METHODS

KEY RESOURCES TABLE

REAGENT or RESOURCE	SOURCE	IDENTIFIER
Antibodies		
METTL3 Ab	Proteintech	Cat# 150731-1-AP; RRID: AB_2142033
MYC Ab	Cell signalingTechnology	Cat# 5605S; RRID:AB_1903938
Actin Ab	Sigma Aldrich	Cat# A3854; RRID:AB_262011
Gr1-APC cloneRB6-8C5	Thermo Fisher Scientific	Cat# 17-5931-82; RRID:AB_469476
Mac1-PB clone M1/70	Biolegend	Cat# 101224; RRID:AB_755986
c-Kit APCCy7 clone2B8	Biolegend	Cat# 105826; RRID:AB_1626278
B220-PeCy7 clone RA3-6B2	BD Biosciences	Cat# 552772; RRID:AB_394458
CD19-PeCy5 clone eBio1D3	Thermo Fisher Scientific	Cat# 15-0193-83; RRID:AB_657673
IgM APC clone RMM-1	Biolegend	Cat# 406509; RRID:AB_315059
CD3e-PB clone 145-2C11	Thermo Fisher Scientific	Cat# 48-0031-80; RRID:AB_10733280
CD4 PE clone GK1.5	BD Biosciences	Cat# 557308; RRID:AB_396634
CD8 FITC clone 53-6.7	BD Biosciences	Cat# 553031; RRID:AB_394569
CD34-FITC clone RAM34	eBioscience	Cat# 11-0341-85; RRID:AB_465022
Sca1-PB clone E13-161.7	Biolegend	Cat# 122520; RRID:AB_2143237
CD150-APC clone TC15-12F12.2	Biolegend	Cat# 115910; RRID:AB_493460
CD48-PE clone HM48-1	BD Biosciences	Cat# 557485 RRID:AB_396725
FcgRIIb-PeCy7 clone 2.4G2	BD Biosciences	Cat# 560829 RRID:AB_10563207
CD41-PE clone MWReg30	BD Biosciences	Cat# 558040 RRID:AB_397004
Ter119-PeCy5 clone TER-119	Thermo Fisher Scientific	Cat# 15-5921-82 RRID:AB_468810
CD71-FITC clone R17217	Thermo Fisher Scientific	Cat# 11-0711-81 RRID:AB_465123
CD45.1 Pe-CF594 clone A20	BD Biosciences	Cat# 562452 RRID:AB_11152958
CD45.2 Alexa 700 clone 104	Thermo Fisher Scientific	Cat# 56-0454-82 RRID:AB_657752
CD3-PeCy5	Invitrogen	Cat# 15-0031-83 RRID:AB_468691
CD4-PeCy5	Invitrogen	Cat# 15-0041-83 RRID:AB_468696
CD8-PeCy5	Invitrogen	Cat# 15-0081-83 RRID:AB_468767
Gr1-PeCy5	Invitrogen	Cat# 15-5931-82 RRID:AB_468813
B220- PeCy5	Invitrogen	Cat# 15-0452-83 RRID:AB_468756
CD19- PeCy5	Invitrogen	Cat# 15-0193-83 RRID:AB_657673
Ki67 –FITC	Biolegend	Cat# 652410 RRID: AB_2562141
NUMB Ab	Abcam	Cat# Ab4147 RRID:AB_304320
m^6A Ab	Abcam	Cat# Ab151230 RRID:AB_2753144
Chemicals, Peptides, and Recombinant Proteins		
pIpC HMW	InVivogen	Cat# Vac-Pic
MitoTracker Green	Invitrogen	Cat# M7514
Pyronin Y	Sigma	Cat# 213519
Murine SCF	Peprotech	Cat# 250-03
Murine IL-3	Peprotech	Cat# 213-13
Murine IL-6	Peprotech	Cat# 216-16
Murine TPO	Peprotech	Cat# 315-14
Murine FLT3L	Peprotech	Cat# 250-31L
MethoCult M3434	Stem Cell Technologies	Cat# 03434
SFEM medium	Stem Cell Technologies	Cat# NC9753895

(*Continued on next page*)

Continued		
REAGENT or RESOURCE	SOURCE	IDENTIFIER
O-Propargyl-puromycin (OP-Puro)	Jena Bioscience	Cat# NU-931-05
Actinomycin D	Sigma	Cat# 50-76-0
Critical commercial assays		
RNeasy Plus Micro Kit	QIAGEN	Cat# 74034
Murine CD117 MicroBeads Kit	Miltenyi Biotec	Cat# 130091224
Verso cDNA Synthesis Kit	Thermo Fisher Scientific	Cat# AB1453-B
Power SYBR Green PCR Master Mix	Thermo Fisher Scientific	Cat# 4367659
Click-iT Flow Cytometry Assay kit	Thermo Fisher Scientific	Cat# C10418
RNAscope multiplex fluorescent detection kit	Advanced Cell Diagnostics	Cat# 320851
Deposited Data		
Single cell RNA-sequencing data and bulk RNA-sequencing data	National Center for Biotechnology Information (NCBI) Gene Expression Omnibus (GEO)	GSE132357
Experimental Models: Strains		
Mouse: *Mettl3* f/f Mx1-Cre mice	This paper	N/A
Mouse: C57BL/6J	The Jackson Laboratory	Stock No: 000664
B6.SJL-Ptprc < a > /Boy	Taconic Biosciences	Stock No: 4007
Oligonucleotides		
Genotyping primers-Forward	ACCACAACAGCCAAGGAACA	N/A
Genotyping primers-Reverse	CCGGAGCTCTGAAACCTTGT	N/A
Myc-Forward	GCTGTTTGAAGGCTGGATTTC	N/A
Myc-Reverse	GATGAAATAGGGCTGTACGGAG	N/A
Mettl3-Forward	AAGGAGCCGGCTAAGAAGTC	N/A
Mettl3-Reverse	TCACTGGCTTTCATGCACTC	N/A
Actin-Forward	ACCAACTGGGACGACATGGAGAAG	N/A
Actin-Reverse	TACGACCAGAGGCATACAGGGACA	N/A
Recombinant DNA		
MSCV-MYC-IRES-GFP	This paper	N/A
MSCV-FLAG-METTL3-IRES-GFP	This paper	N/A
MSCV- FLAG-METTL3-CD-IRES-GFP	This paper	N/A
Software and Algorithms		
ImageJ version 2.0.0	ImageJ	N/A
FlowJo software (version10.2)	FlowJo	N/A
GraphPad Prism 7	GraphPad Software	N/A
R version 3.5.2 (2018-12-20)	R development core team, 2018	N/A
Rstudio 1.1.456	Rstudio, Inc.	N/A
cellrangerRkit 2.0.0	10x Genomics	https://www.r-project.org
Seurat 2.3.4	Raul Satija laboratory at New York Genome Center	https://www.rstudio.com/
dplyr 0.8.1	Romain François, Lionel Henry and Kirill Müller	software@10xgenomics.com

LEAD CONTACT AND MATERIALS AVAILABILITY

Further information and requests for reagents may be directed to, and will be fulfilled by the corresponding author Michael G Kharas (kharasm@mskcc.org).

EXPERIMENTAL MODEL AND SUBJECT DETAILS

Mice

Mettl3 *flox/flox* mice were generated by inserting loxP sites spanning the fourth exon of Mettl3 via homologous recombination base on construction taken from Knockout Mouse Project Repository (KOMP). We next crossed Mettl3 *flox/flox* mice with Mx1-Cre mice to

obtain induced hematopoietic conditional knockout mice. Deletion of Mettl3 was initiated using pIpC HMW (InVivogen, Vac-Pic) by intraperitoneal injections at a dose of 10 mg/kg on 2 consecutive days as showed previously (Liu et al., 2015). Mice used for this experiment were 8 to 12 weeks of age. Both male and female mice were used. All mice were housed on a 12:12 hr light:dark cycle at 25°C and received water and chow *ad libitum*. All of the animal experiments were approved under the Institutional Animal Care and Use Committee.

METHOD DETAILS

Noncompetitive Transplant

Noncompetitive transplants were performed as previously described(Park et al., 2014). Briefly, in the primary transplant, 10^6 whole bone marrow cells from *Mettl3 cKO* mice or littermate *Mettl3 f/f* mice (3 weeks post pIpC) were injected into lethally irradiated B6SJL congenic CD45.1 recipients. In the cell-autonomous transplants, we transplant 10^6 whole BONE MARROW cells from 8-12 weeks old *Mettl3 flox/flox*, *Mx1-Cre+* or *Mx1-Cre-* mice into lethally irradiated B6SJL congenic CD45.1 recipients. After 6 weeks of engraftment, these transplanted mice were treated with pIpC as shown previously. All recipient mice used were 6-8 weeks old. All animals were randomly assigned to the experimental groups. For chimerism, either peripheral blood or bone marrow cells was extracted and subjected to flow cytometry at different time points.

PCR and Quantitative RT-PCR

Genomic DNA from *Mettl3 f/f* and *Mettl3 cKO* whole bone marrow cells was isolated by using genomic DNA extraction kit (QIAGEN) and used as template for PCR to genotype. Primers are Forward: ACCACAACAGCCAAGGAACA ; Reverse: CCGGAGCTCT GAAACCTTGT. For qRT-PCR, total RNA was extracted from cells using TRIZOL (Life Technologies) following the standard manual. Equal amount of RNA from samples was reverse transcribed into cDNA with Verso cDNA Synthesis Kit (Thermo), and qPCR was performed using an ABI 7500 sequence detection system using primers together with SYBR green master mix (ABI systems). Primers are listed below:

Myc: Forward: GCTGTTTGAAGGCTGGATTTC
Reverse: GATGAAATAGGGCTGTACGGAG
Mettl3: Forward: AAGGAGCCGGCTAAGAAGTC
Reverse: TCACTGGCTTTCATGCACTC
Actin: Forward: ACCAACTGGGACGACATGGAGAAG
Reverse: TACGACCAGAGGCATACAGGGACA

Flow Cytometry and Cell Sorting

Bone marrow or spleen cells were harvested and subjected to red blood cell lysis. To measure HSPC compartments, cells were stained with following cocktail: Linage marker (CD3 (15-0031-83), CD4(15-0041-83), CD8(15-0081-83), Gr1(15-5931-82), B220(15-0452-83), CD19(15-0193-83) and Ter119(15-5921-82))- PE-Cy5(Invitrogen, eBioscience), cKit-APC-Cy7 (BioLegend, 105826), Sca-1-Pacific Blue (BioLegend, 122520), CD150-APC (BioLegend, 115910), CD48-PE (BD Bioscience, 557485), CD34-FITC (eBioscience, 11-0341-85), CD16/32-PE-Cy7 (BD Bioscience, 560829). To monitor linage cells differentiation cells were stained with cocktail including Gr1-APC (Invitrogen, 17-5931-82), Mac1-Pacific Blue (BioLegend, 101224), Ter119-PE-Cy5 (Invitrogen, 15-5921-82), CD71-FITC (Invitrogen, 11-0711-81), CD41-PE (BD Bioscience, 558040) or cocktail containing CD3-Pacific Blue (eBioscience, 48-0031-80), CD4-PE (BD Bioscience, 557308), B220-PE-Cy7 (BD Bioscience, 552772), CD19-PE-Cy5 (Invitrogen, 15-0193-83), IgM-APC (BioLegend, 406509), CD43-FITC (BD Bioscience, 553270). For transplanted mice, we added CD45.1-PE-Txase Red (BD Bioscience, 562452) and CD45.2-A700 (Invitrogen, 56-0454-82) to distinguish donor and recipient cells. For cell cycle analyses, Ki67/Hoechst staining was performed according to manufacturer's recommendation (BD Biosciences). For PY/Hoechst staining, bone marrow cells stained with HSC surface markers (Linage marker (CD3, CD4, CD8, Gr1, B220, CD19 and Ter119)-PE-Cy5, cKit-APC-Cy7, Sca-1-PECy7 (BioLegend, 122514), CD150-APC, CD48-FITC (BioLegend, 103404)) were resuspended in 500ul NASS buffer (1 phosphate citrate tablet (sigma), 0.9g EDTA, 0.45 g NaCl, 0.25 g BSA in 50ml ddH2O), 3.3ul diluted Hoechst (1:10 in NASS) was added followed by 30mins in room temperature. Samples were then incubated on ice for 5 mins to stop reaction. 2.5ul of diluted PY (1:100 of 10mg/ml PY stock in NASS) was added to samples. Incubate for 10mins at 4 degree. Wash the samples before analysis. For mitochondrial mass and activity, BMCs were incubated with 100nM MitoTracker Green (Invitrogen) or 50nM DilC5 (Thermo Fisher) for 30 min at 37°C in the dark after cell surface staining (Linage marker (CD3, CD4, CD8, Gr1, B220, CD19 and Ter119)- PE-Cy5, cKit-APC-Cy7, Sca-1-Pacific Blue, CD150-APC/CD150 FITC, CD48-PE). Cells were analyzed on a BD FACS LSR or Fortessa instrument. For HSPC(LSK) or HSC (LSK, CD150+CD48-) cell sorting, bone marrow cells were harvested and incubated with MACS beads (CD117, Miltenyi Biotec, 130-091-224). Then enriched c-Kit+ cells were collected by running AutoMACS (Miltenyi Biotec) according to the manufacturer's instructions. The cells were then stained with cocktail: Linage marker (CD3, CD4, CD8, Gr1, B220, CD19 and Ter119)- PE-Cy5, cKit-APC-Cy7, Sca-1-Pacific Blue, CD150-APC, CD48-PE. Specific cell population was sorted on BD Aria machine.

Peripheral Blood Analysis

Peripheral blood was collected from the retroorbital cavity using a heparinized glass capillary tube. Complete peripheral blood count analysis including a differential blood count was obtained by using Hemavet (Drew Scientific). For flow cytometry, peripheral blood was treated by red blood cell lysis to remove red blood cells and then applied to flow as showed earlier.

Western-Blot

LSK cells were sorted from *Mettl3 f/f* and *Mettl3 cKO* bone marrow cells following protocol described before. 50,000 cells were then lysed in 30 μL 1 × Laemmli protein loading buffer and boiled for 5 min. Whole-cell lysates were run on a 4%–15% gradient SDS–PAGE and transferred to a nitrocellulose membrane. Membranes were probed with the METTL3 (Proteintech, 150731-1-AP) and ACTIN (Sigma, A3854) antibody.

Determination of Relative m^{6}A Levels

Relative levels of global m^{6}A was determined by thin-layer chromatography (TLC), as described previously(Vu et al., 2017a). Briefly, poly(A)-purified RNA was digested with 2 U ribonuclease T1 for 2 h at 37°C in the presence of RNaseOUT (Invitrogen) first. Next, we labeled digested RNA at 5′ with [γ-32P] ATP. After removal of γ phosphate of ATP by apyrase (NEB), labeled RNA was purified by phenol-chloroform extraction and ethanol precipitation and digested to single nucleotides nuclease. 1 mL of released 5′ monophosphates was analyzed on glass-backed PEI-cellulose plates (Merck-Millipore) and exposed to a storage phosphor screen (GE Healthcare Life Sciences), as described previously. The relative m^{6}A was calculated as a percentage of the total of A, C and U spots which is quantified with ImageJ, as described previously (Mauer et al., 2017).

Colony Assay

10,000 whole *Mettl3 f/f* or *Mettl3 cKO* bone marrow cells were plated in in M3434 methylcellulose media (STEMCELL Technologies, 03434), and colonies were scored at 10 days post plating, respectively.

Competitive Transplant

HSC and MPP1 cells from *Mettl3 f/f* or *Mettl3 cKO* mice were sorted following protocol described above. 500 sorted HSC and MPP1 cells plus 500K CD45.1 whole bone marrow cells as support cells were injected into lethally irradiated B6SJL congenic CD45.1 recipients directly after cell sorting. For chimerism, either peripheral blood or bone marrow cells was extracted and subjected to flow cytometry at different time points.

HSPC Cell Sorting, Cell Culture, Retroviral Infection, and Transplant

HSPC(LSK) cells from *Mettl3* f/f or *Mettl3 cKO* mice were sorted following protocol described above. Sorted LSK cells were cultured in the SFEM medium (STEMCELL Technologies, NC9753895) supplemented with murine cytokines (50 ng/ml SCF, 10 ng/ml IL-3, and 10 ng/ml IL-6, 10ng/ml TPO and 20 ng/ml FLT3L, PeproTec). Cells were then transduced with high-titer concentrated retroviral suspensions in the presence of 4 μg/ml polybrene and followed with spin infection for 1.5 hr. Next day, second round of transduction was performed as described. For transplant, 10,000 LSK cells plus 500K CD45.1 whole bone marrow cells were injected into lethally irradiated B6SJL congenic CD45.1 recipients. For chimerism, either peripheral blood or bone marrow cells was extracted and subjected to flow cytometry at different time points.

O-Propargyl-puromycin (OP-Puro) Flow Analysis

Protein synthesis rate was assessed by O-Propargyl-puromycin (OP-Puro) as described previously(Vu et al., 2017b). *Mettl3 f/f* and *Mettl3 cKO* HSC cells were sorted and treated with 50 μM O-propargyl-puromycin (OP-Puro; NU-931-05, Jena Bioscience) for 1 hour. Cells were washed once, collected, and then subjected to processing using the Click-iT Flow Cytometry Assay kit (C10418, Invitrogen) following the manufacturer's instructions. Labeled cells were analyzed using a BD Fortessa instrument.

Immunofluorescence

HSCs were sorted from *Mettl3 f/f* and *Mettl3 cKO* mice following protocol shown before. We cultured the sorted HSCs with SFEM media (STEMCELL Technologies, NC9753895) containing 10 ng/ml heparin, 10 ng/ml SCF, 20 ng/ml TPO, 20 ng/ml IGFII, and 10 ng/ml FGF, PeproTec) in 96 round-bottom wells for 16 h and then treated cells with 10 nM Nocodazole for 24 h. After incubation, cells were fixed with 4% paraformaldehyde 15 mins at room temperature and permeabilized with cold methanol. Fixed HSCs were then cytospun onto glass slides and were blocked for 1h followed with staining on slides with anti-NUMB (Abcam, ab4147), anti-MYC (Cell Signaling, 5605) and secondary Ab (donkey anti–goat Alexa fluor 488, Invitrogen, A11055; donkey anti–rabbit Alexa fluor 568, Invitrogen, A10042; Molecular Probes) with DAPI counterstaining. We evaluate symmetric and asymmetric percentages based on the fluorescence signal intensity of each cell acquired by Axio Imager M2 microscope (Carl Zeiss) and quantified by FIJI. Thresholds to determine NUMB high/low/asymmetric were set for experimental replicates. Briefly, both of daughter cells with high NUMB staining or average staining intensity is above NUMB high threshold and there is less than 2-fold difference in the daughter pairs, this condition was counted as symmetric commitment. Daughter pair cells were scored as a symmetric renewal

division when both of them were low or no staining or average staining intensity is below NUMB high threshold and there is less than 2-fold difference in the daughter pairs. If else, the division was considered an asymmetric division(Kharas et al., 2010).

RNA-FISH in Conjugation with Fluorescent Immunostaining

Sorted HSCs were cultured in SFEM media and treated with Nocodazole as shown above. HSC cells were then fixed with 4% paraformaldehyde and permeabilized with cold methanol. Fixed HSCs were then cytospun onto glass slides. RNA *in situ* hybridization was performed using RNAscope multiplex fluorescent detection kit according to the manufacturer's instructions (Advanced Cell Diagnostics). RNAscope probes targeting mouse *Myc* was designed and produced by ACDbio. After the in situ hybridization was completed, slides were washed twice and subjected to immunostaining as shown above.

RNA Stability Assay

Sorted HSCs were cultured in SFEM media supplemented with cytokines as shown above. After overnight culture, HSCs were treated with 5 μM actinomycin D (Sigma) for inhibition of mRNA transcription. Cells were collected at 0 min, 10 min, 20 min or 40 min post treatment, and total RNA was extracted and used for qRT-PCR.

Electroporation Transfection

Neon nucleofection of HSPCs was performed as described(Gundry et al., 2016). HSCs were sorted and cultured in the SFEM medium for 1-3 hours before transfection. 1ug Plasmids or 100pmol siRNAs were electroporated into 100,000 HSCs or LSKs by using Neon transfection system (Thermo Fisher Scientific) under a condition:1700V, 20ms, 1 pulse. If higher numbers of cells were needed, multiple electroporations were performed (e.g., 6 electroporations of 100,000 LSKs for 600,000 total cells).

m^{6}A-seq Peak Enrichment Analysis

Previously published data of m^{6}A-seq and input RNA-seq from mouse LT-HSCs, ST-HSCs, and MPPs were downloaded from NCBI GEO (GSE107957). PCR duplicates were removed using the pyDuplicateRemover.py script of the pyCRAC tool suite (version 1.2.2.3). Deduplicated sequences were then aligned to the mm10 mouse genome build using bowtie2 (version 2.3.4.2) (bowtie2 -x mm10 -N 0 –trim5 3). Significantly enriched m^{6}A peaks were determined using the R/Bioconductor package exomePeak.

MeRIP-qPCR

MeRIP-qPCR was performed as described previously(Vu et al., 2017a). Briefly, total RNA was isolated from sorted LSKs cells (from 3 *Mettl3 cKO* or control mice) by Trizol and poly(A)$^+$ RNA was isolated using Dynabeads Oligo-(dT)25 magnetic beads (ThermoFisher Scientific). 5 μg anti-m^{6}A antibody (Abcam, ab151230) was pre-bound to Protein A/G magnetic beads (Pierce) in IP buffer (20-mM Tris pH 7.5, 140-mM NaCl, 1% NP-40, 2-mM EDTA) for 1h. 1 μg Poly(A)$^+$ RNA was mixed with 400 μl of IP buffer and added to the Protein A/G beads for 2 hours at 4°C. Samples were washed twice in low-salt-wash buffer (10-mM Tris pH 7.5, 5 mM EDTA), twice with high-salt-wash buffer (20-mM Tris pH 7.5, 1-M NaCl, 1% NP-40, 0.5% sodium deoxycholate, 0.1% SDS, 1-mM EDTA) and twice with RIPA buffer (20-mM Tris pH 7.5, 150-mM NaCl, 1% NP-40, 0.5% sodium deoxycholate, 0.1% SDS, 1-mM EDTA). RNA was eluted from the beads by incubating with 200 μl 0.5 mg/ml N6-methyladenosine 5-monophosphate sodium salt (Sigma Aldrich) for 1h at 4°C. Following ethanol precipitation, input and eluted poly(A)$^+$ RNA was reverse-transcribed using Superscript III with random hexamers, and enrichment of m^{6}A-containing transcripts was determined by quantitative PCR.

RNA-Seq

3 replicates (from 3 different mice) of HSC, MPP1, MPP2 and MPP4 cells were sorted from *Mettl3* f/f and *Mettl3 cKO* mice base on cell surface marker. RNA was extracted from bulk cells using the SMARTer RNA extraction method for minimal cells RNA extraction. After amplification, cDNA was subjected to automated Illumina paired-end library construction. Libraries were sequenced on Illumina HiSeq2000 instruments with paired reads of 50 bp in length per sample. Sequence data were aligned using the tophat software to the GRCh37-lite human reference genome. Fragments Per Kilobase of transcript per Million mapped reads were calculated using the cufflink software. Differentially expressed genes were identified as those with FPKM greater than 1 for *Mettl3* f/f or *Mettl3 cKO* showing differential expression greater than twofold (up or down) with a Benjamini–Hochberg corrected p value less than 0.05.

Single-Cell RNA-Seq

Single-cell RNA-seq data processing, alignment, cell type classification and clustering: 10x data were processed using Cell Ranger 2.1.0 with default parameters. Reads were aligned to the mouse reference mm10. The Seurat package(Butler et al., 2018) was used to perform unbiased clustering of the cells bone marrow Lin$^-$, c-Kit$^+$ sorted hematopoietic progenitors. Briefly, cells with < 200 detected genes or percentage of mitochondrial reads > 20% were filtered out. In addition, cells that showed lower number of genes than expected from the number of UMIs detected (Figure S4B) were filtered out as low-quality cells. The data were log normalized using a scale factor of 10,000. Potential confounders (e.g., number of UMI per cell, the proportion of mitochondrial genes and proportion of ribosomal genes) were regressed out of the data before principle component analysis (PCA) was performed using variable genes. JackStraw method was used to determine the statistically significant PCs to be used for graph-based clustering. t-SNE was used to visualize the clusters. Cell types were classified according to expression of previously reported marker genes(Paul et al., 2015).

Pseudotime ordering was performed using Monocle(Trapnell et al., 2014), setting the origin of pseudotime in the cell state containing the highest fraction of cells from the HSC cluster.

QUANTIFICATION AND STATISTICAL ANALYSIS

Data were processed using GraphPad Prism v.7. All analyses were performed using two-tailed Student's t tests, except where stated otherwise. Graphs and error bars reflect means ± s.e.m., except where stated otherwise. In all corresponding figures, * represents $p < 0.05$. ** represents $p < 0.01$. *** represents $p < 0.001$. ns represents $p > 0.05$. Replicate information is indicated in the figures.

DATA AND CODE AVAILABILITY

The single cell RNA-seq and bulk RNA-seq data have been deposited in the Gene Expression Omnibus with GEO: GSE132357.

Cell Reports, Volume *28*

Supplemental Information

m^6A RNA Methylation Maintains Hematopoietic Stem Cell Identity and Symmetric Commitment

Yuanming Cheng, Hanzhi Luo, Franco Izzo, Brian F. Pickering, Diu Nguyen, Robert Myers, Alexandra Schurer, Saroj Gourkanti, Jens C. Brüning, Ly P. Vu, Samie R. Jaffrey, Dan A. Landau, and Michael G. Kharas

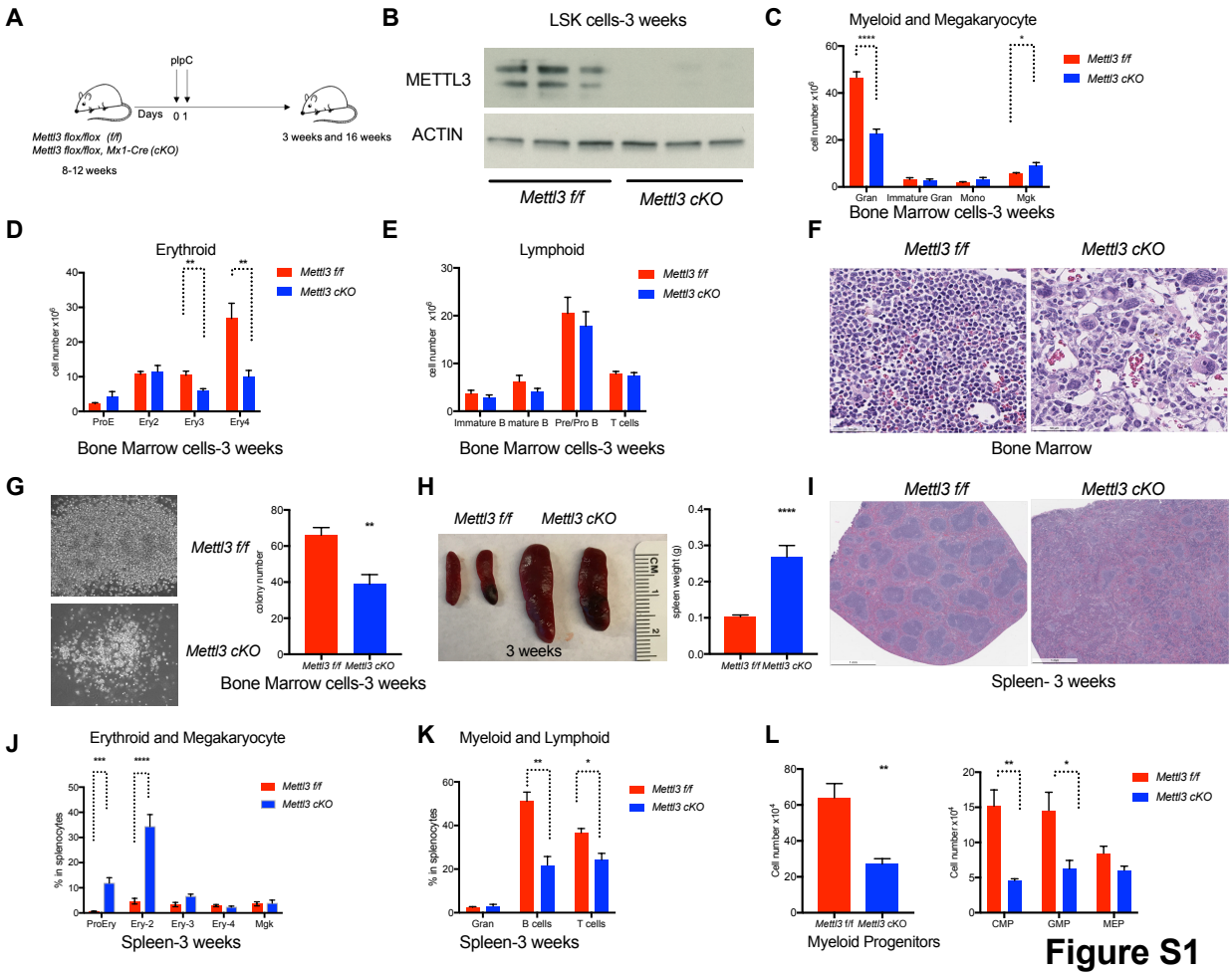
A
pIpC
Days 0 1
Mettl3 flox/flox (f/f)
Mettl3 flox/flox, Mx1-Cre (cKO)
8-12 weeks
3 weeks and 16 weeks
B
LSK cells-3 weeks
METTL3
ACTIN
Mettl3 f/f
Mettl3 cKO
C
Myeloid and Megakaryocyte
cell number x10^6
Gran
Immature Gran
Mono
Mgk
Mettl3 f/f
Mettl3 cKO
Bone Marrow cells-3 weeks
D
Erythroid
cell number x10^6
ProE
Ery2
Ery3
Ery4
Mettl3 f/f
Mettl3 cKO
Bone Marrow cells-3 weeks
E
Lymphoid
cell number x10^6
Immature B
mature B
Pre/Pro B
T cells
Mettl3 f/f
Mettl3 cKO
Bone Marrow cells-3 weeks
F
Mettl3 f/f
Mettl3 cKO
Bone Marrow
G
Mettl3 f/f
Mettl3 cKO
colony number
Mettl3 f/f
Mettl3 cKO
Bone Marrow cells-3 weeks
H
Mettl3 f/f
Mettl3 cKO
3 weeks
spleen weight (g)
Mettl3 f/f
Mettl3 cKO
I
Mettl3 f/f
Mettl3 cKO
Spleen- 3 weeks
J
Erythroid and Megakaryocyte
% in splenocytes
ProEry
Ery-2
Ery-3
Ery-4
Mgk
Mettl3 f/f
Mettl3 cKO
Spleen-3 weeks
K
Myeloid and Lymphoid
% in splenocytes
Gran
B cells
T cells
Mettl3 f/f
Mettl3 cKO
Spleen-3 weeks
L
Cell number x10^4
Mettl3 f/f
Mettl3 cKO
Myeloid Progenitors
Cell number x10^4
CMP
GMP
MEP
Mettl3 f/f
Mettl3 cKO

Figure S1

Supplementary Figure 1. m^{6}A is essential for normal hematopoiesis. Related to Figure 1.

All samples were collected from mice at 3 weeks post pIpC administration. **(A)** Schematic diagram of the experimental procedure for analyzing *Mettl3 f/f* and *Mettl3 cKO* mice. **(B)** Immunoblot to determine METTL3 expression using sorted LSK cells. **(C-E)** Myeloid, megakaryocytes, erythroid, and lymphoid lineage differentiation in BM was determined by flow cytometry base on different cell surface markers. Erythroblast (ProE, Ter119-CD71+; Ery2, Ter119+CD71+; Ery3, Ter119+CD71^{mid}; Ery4, Ter119+CD71-), Gran (Granulocyte, Gr1+Mac1+), Immature Granulocyte(Mac1+Gr1^{mid}), Monocyte(Mac1+Gr1-), Megakaryocytes (Mgk, CD41+), Immature B cells(B220+IgM+), Pre/Pro B cells (B220+IgM-), Mature B cells (B220^{hi}IgM+), T cells (CD3+). n=11. **(F)** Representative images show H&E-stained cross sections of BM isolated from the *Mettl3 f/f* and *Mettl3 cKO* mice. **(G)** *Mettl3* depleted BM formed fewer and smaller colonies. *Mettl3 f/f* and METTL3 depleted BM cells were plated in methylcellulose cultures, supplemented with cytokines. Left: Representative images of flox/flox and cKO colony. Right: Colonies were scored 10 days after plating. n =9,7. **(H)** Splenomegaly is observed in cKO mice three weeks post pIpC administration. Left: representative image of spleens from indicated mice. Right: measurement of spleen weight from *Mettl3 f/f* and *Mettl3 cKO* mice. n=11. **(I)** Representative images show H&E-stained cross sections of spleens isolated from the *Mettl3 f/f* and *Mettl3 cKO* mice. **(J, K)** Erythroid, myeloid and lymphoid cells were determined by flow cytometry in *Mettl3 f/f* and *Mettl3 cKO* spleens. Cell population was determined by cell surface marker. n=8. **(L)** Absolute numbers of myeloid progenitor (MP, Lin-ckit+Sca1-), CMP(Lin-cKit+Sca1-CD34+FcrR-), GMP (Lin-cKit+Sca1-CD34+FcrR+) and MEP(Lin-cKit+Sca1-CD34-FcrR-) in *Mettl3* f/f and *Mettl3* cKO BM. n=10, 6. Mean and SEM are shown (*, $P < 0.05$; **, $P < 0.01$; ***, $P < 0.001$, ****, $P < 0.0001$).

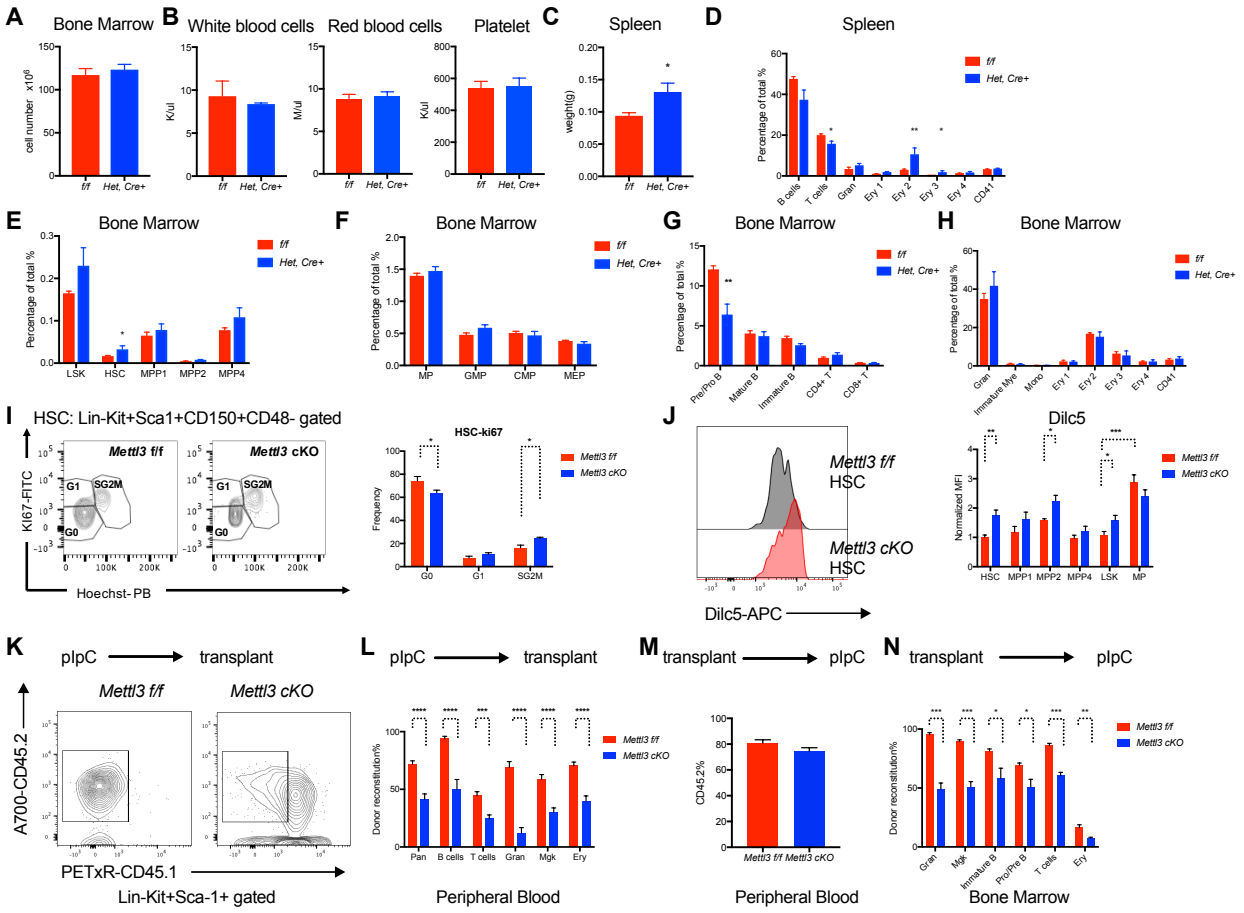
A
Bone Marrow
cell number x10^6
f/f
Het, Cre+
B
White blood cells
K/ul
Red blood cells
M/ul
Platelet
K/ul
C
Spleen
weight(g)
D
Spleen
Percentage of total %
B cells
T cells
Gran
Ery 1
Ery 2
Ery 3
Ery 4
CD41
E
Bone Marrow
LSK
HSC
MPP1
MPP2
MPP4
F
Bone Marrow
MP
GMP
CMP
MEP
G
Bone Marrow
Pre/Pro B
Mature B
Immature B
CD4+ T
CD8+ T
H
Bone Marrow
Gran
Immature Mye
Mono
Ery 1
Ery 2
Ery 3
Ery 4
CD41
I
HSC: Lin-Kit+Sca1+CD150+CD48- gated
Mettl3 f/f
Mettl3 cKO
G1
SG2M
G0
KI67-FITC
Hoechst- PB
HSC-ki67
Frequency
G0
G1
SG2M
J
Mettl3 f/f
HSC
Mettl3 cKO
HSC
Dilc5-APC
Dilc5
Normalized MFI
HSC
MPP1
MPP2
MPP4
LSK
MP
K
pIpC
transplant
Mettl3 f/f
Mettl3 cKO
A700-CD45.2
PETxR-CD45.1
Lin-Kit+Sca-1+ gated
L
pIpC
transplant
Donor reconstitution%
Pan
B cells
T cells
Gran
Mgk
Ery
Peripheral Blood
M
transplant
pIpC
CD45.2%
Mettl3 f/f
Mettl3 cKO
Peripheral Blood
N
transplant
pIpC
Donor reconstitution%
Gran
Mgk
Immature B
Pro/Pre B
T cells
Ery
Bone Marrow

Figure S2

Supplementary Figure 2. *Mettl3* required for HSC reconstitution capacity. Related to Figure 2.

(A) Whole bone marrow cellularity in *Mettl3 f/f* and *Het,Cre+ (Mettl3 f/-, Mx1-Cre)* mice. n=4. **(B)** Whole blood counts of white blood cell (WBCs), red blood cells (RBCs), platelets (PLT) of *Mettl3 f/f* and *Het,Cre+* mice. n=4. **(C)** Spleen weight of *Mettl3 f/f* and *Het,Cre+* mice. n=4. **(D)** Mature lineage cells were determined by flow cytometry in *Mettl3 f/f* and *Het,Cre+* spleens base on cell surface marker as shown in **Supplementary Figure1**. n=4. **(E, F)** Frequency of hematopoietic stem and progenitor compartments (LSK, HSC, MPP1, MPP2 and MPP4) and myeloid progenitors (MP, CMP, GMP and MEP) in *Mettl3 f/f* and *Het,Cre+* mice bone marrow. n=4. **(G, H)** Erythroid, myeloid, megakaryocytes and lymphoid lineage differentiation in *Mettl3 f/f* and *Het,Cre+* mice were assessed by flow cytometry base on cell surface markers. n=4. **(I)** *Mettl3 cKO* HSC cells are more proliferative. Representative flow cytometry plots and quantification of *Mettl3 f/f* and *Mettl3 cKO* HSC cell cycle by Ki67 staining. n=5. **(J)** Increased mitochondrial activity in *Mettl3 cKO* HSCs. Left: representative histograms of Dilc5 staining in *Mettl3 f/f* and *Mettl3 cKO* HSCs. Right: Mitochondrial membrane potential in HSPC compartments was assessed by Dilc5 staining quantified by flow cytometry. n=5. **(K)** Representative flow cytometry of surface markers to indicate engraftment of CD45.2 donor cells in LSK population from non-competitive transplanted recipient mice. **(L)** *Mettl3 cKO* HSCs have impaired reconstitution capacity. Chimerism of CD45.2 in different lineage cell populations in peripheral blood from non-competitive transplanted recipient mice. n=10. **(M,N)** Cell autonomous transplant experiments. **(M)** Comparable engraftment of *Mettl3 flox/flox*, *Mx1-Cre-* and *Mx1-Cre+* recipient pre-pIpC. Chimerism of CD45.2 donor cells in peripheral blood from recipient mice was analyzed before pIpC injection. n=15. **(N)** CD45.2 chimerism analysis of myeloid, erythroid and lympoid cells from recipient mice. Cell compartment is determined by cell surface marker as showed previously. n=5. Mean and SEM are shown (*, $P < 0.05$; **, $P < 0.01$; ***, $P < 0.001$, ****, $P < 0.0001$).

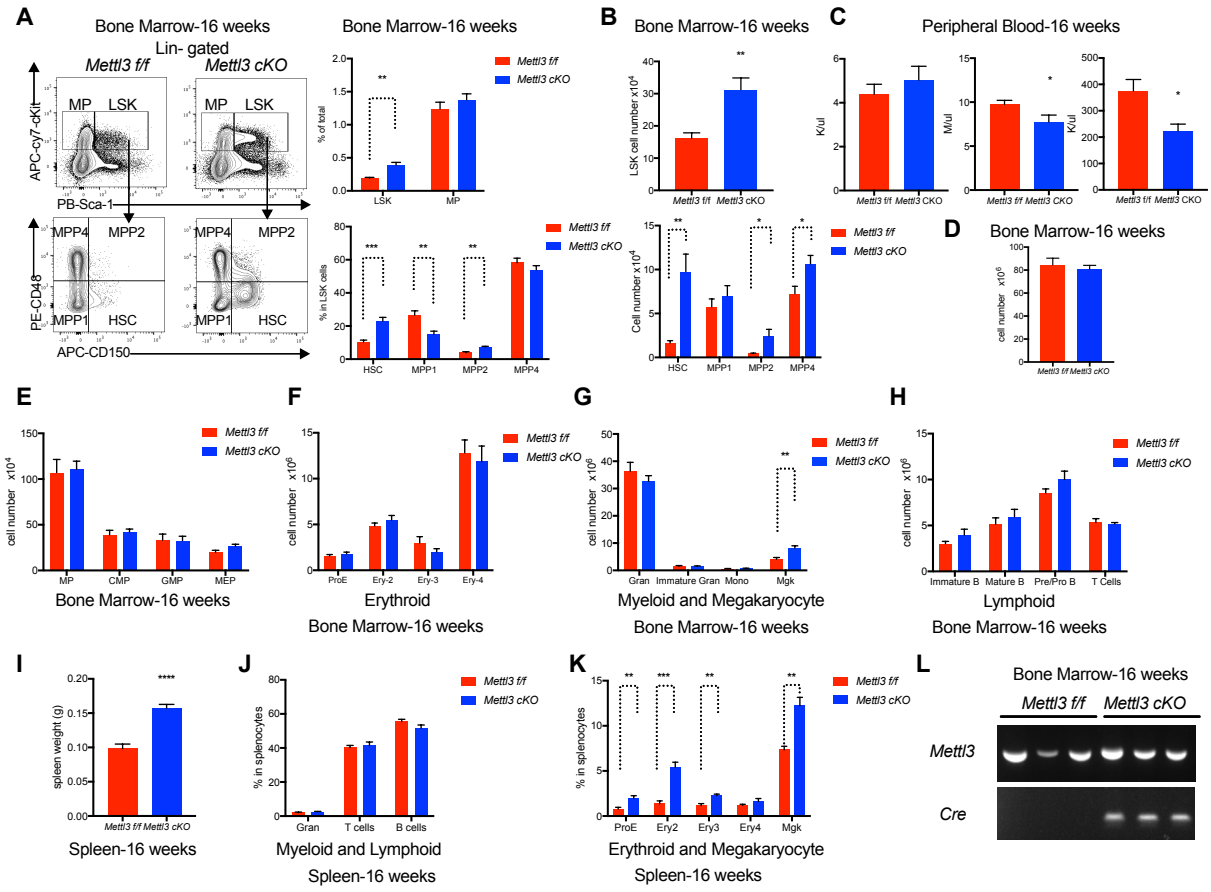
A
Bone Marrow-16 weeks
Lin- gated
Mettl3 f/f
Mettl3 cKO
APC-cy7-cKit
MP
LSK
PB-Sca-1
PE-CD48
MPP4
MPP2
MPP1
HSC
APC-CD150
Bone Marrow-16 weeks
% of total
% in LSK cells
LSK
MP
HSC
MPP1
MPP2
MPP4
B
Bone Marrow-16 weeks
LSK cell number x10⁴
Cell number x10⁴
C
Peripheral Blood-16 weeks
K/ul
M/ul
K/ul
D
Bone Marrow-16 weeks
cell number x10⁶
E
cell number x10⁴
MP
CMP
GMP
MEP
Bone Marrow-16 weeks
F
cell number x10⁶
ProE
Ery-2
Ery-3
Ery-4
Erythroid
Bone Marrow-16 weeks
G
cell number x10⁶
Gran
Immature Gran
Mono
Mgk
Myeloid and Megakaryocyte
Bone Marrow-16 weeks
H
cell number x10⁶
Immature B
Mature B
Pre/Pro B
T Cells
Lymphoid
Bone Marrow-16 weeks
I
spleen weight (g)
Spleen-16 weeks
J
% in splenocytes
Gran
T cells
B cells
Myeloid and Lymphoid
Spleen-16 weeks
K
% in splenocytes
ProE
Ery2
Ery3
Ery4
Mgk
Erythroid and Megakaryocyte
Spleen-16 weeks
L
Bone Marrow-16 weeks
Mettl3 f/f
Mettl3 cKO
Mettl3
Cre

Figure S3

Supplementary Figure 3. HSPC expansion persists in *Mettl3 cKO* mice 16 weeks post pIpC. Related to Figure 3.

All samples used were from *Mettl3 f/f* and *Mettl3 cKO* mice at 16 weeks post pIpC**. (A)** Left: Representative flow cytometry plots of surface markers to indicate the stem and progenitor cell compartments in BM. Right: Frequency of LSK and MP in BM cells and percentage of HSC, MPP1, MPP2 and MPP4 in LSK population. n=6. **(B)** Absolute cell numbers of LSK, HSC and MPPs, from indicated mice at 16 weeks post pIpC as assessed by flow cytometry. n=6. **(C)** Whole blood counts of white blood cell (WBCs), red blood cells (RBCs), platelets (PLT) of *Mettl3 f/f* and *Mettl3 cKO* mice. **(D)** Bone marrow cellularity of *Mettl3 f/f* and *Mettl3 cKO* mice. n=6. **(E)** Absolute cell numbers of progenitor, CMP, GMP and MEP in BM cells. n=6. **(F-H)** Erythroid, myeloid, megakaryocytes and lymphoid lineage differentiation in long-term METTL3 deleted mice were assessed by flow cytometry base on cell surface markers as shown in **Supplementary Figure1.**n=6. **(I)** Measurement of spleen weight from *Mettl3 f/f* and *Mettl3 cKO* mice. n=6. **(J,K)** Erythroid, myeloid and lymphoid cells were evaluated by flow cytometry in splenocytes. n=6. **(L)** Genotyping PCR using genomic DNA from *Mettl3 f/f* and *Mettl3 cKO* mice bone marrow cells at16 weeks post pIpC. Mean and SEM are shown (*, $P < 0.05$; **, $P < 0.01$; ***, $P < 0.001$, ****, $P < 0.0001$).

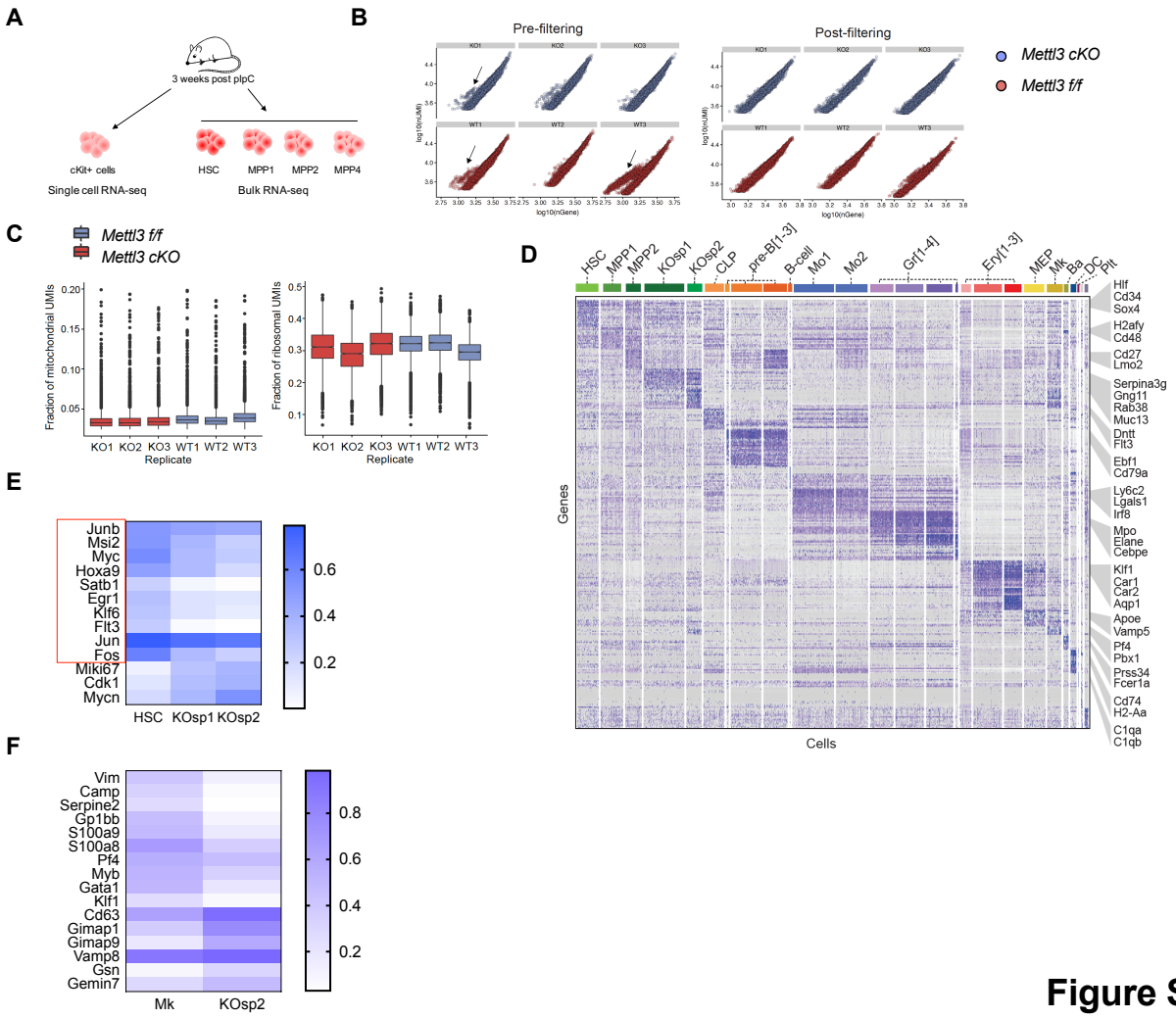
A
3 weeks post plpC
cKit+ cells
Single cell RNA-seq
HSC
MPP1
MPP2
MPP4
Bulk RNA-seq
B
Pre-filtering
Post-filtering
Mettl3 cKO
Mettl3 f/f
C
Mettl3 f/f
Mettl3 cKO
Fraction of mitochondrial UMIs
Fraction of ribosomal UMIs
KO1 KO2 KO3 WT1 WT2 WT3
Replicate
D
HSC
MPP1
MPP2
KOsp1
KOsp2
CLP
pre-B[1-3]
B-cell
Mo1
Mo2
Gr[1-4]
Ery[1-3]
MEP
Mk
Ba
DC
Plt
Genes
Cells
Hlf
Cd34
Sox4
H2afy
Cd48
Cd27
Lmo2
Serpina3g
Gng11
Rab38
Muc13
Dntt
Flt3
Ebf1
Cd79a
Ly6c2
Lgals1
Irf8
Mpo
Elane
Cebpe
Klf1
Car1
Car2
Aqp1
Apoe
Vamp5
Pf4
Pbx1
Prss34
Fcer1a
Cd74
H2-Aa
C1qa
C1qb
E
Junb
Msi2
Myc
Hoxa9
Satb1
Egr1
Klf6
Flt3
Jun
Fos
Miki67
Cdk1
Mycn
HSC KOsp1 KOsp2
F
Vim
Camp
Serpine2
Gp1bb
S100a9
S100a8
Pf4
Myb
Gata1
Klf1
Cd63
Gimap1
Gimap9
Vamp8
Gsn
Gemin7
Mk
KOsp2

Figure S4

Supplementary Figure 4. Loss of *Mettl3* results in new HSC-like clusters base on scRNA-seq. **Related to Figure 4.**

(A) Scheme of experiment strategy for single cell RNA-seq and bulk RNA-seq. **(B)** Filter strategy in three replicates of single cell RNA-seq. **(C)** Number of ribosomal or mitochondrial reads detected for each cell in each replicate. **(D)** Single-cell transcriptome landscape defined by gene expression. Different cell cluster was labeled. **(E)** Heatmap to show differentially expressed genes in *Mettl3 cKO* specific clusters compared to HSC cluster. **(F)** Representative differentially expressed genes between KOsp2 cluster and Megakaryocytes cluster were shown as heat map.

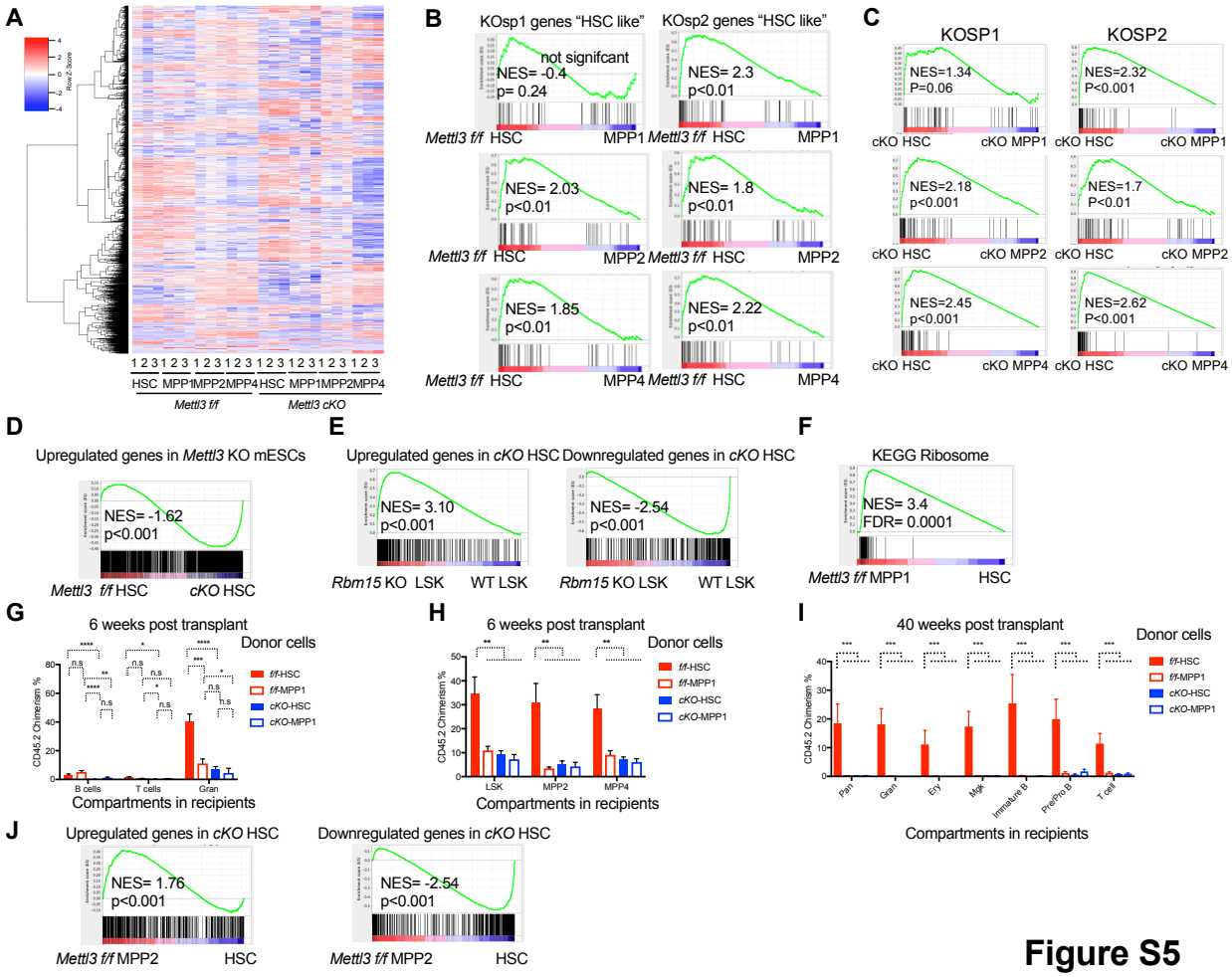
A
Row Z-Score
1 2 3 1 2 3 1 2 3 1 2 3 1 2 3 1 2 3 1 2 3 1 2 3 1 2 3 1 2 3
HSC MPP1 MPP2 MPP4 HSC MPP1 MPP2 MPP4
Mettl3 f/f
Mettl3 cKO
B
KOsp1 genes "HSC like"
KOsp2 genes "HSC like"
not signifcant
NES= -0.4
p= 0.24
NES= 2.3
p<0.01
Mettl3 f/f HSC
MPP1
NES= 2.03
p<0.01
NES= 1.8
p<0.01
MPP2
NES= 1.85
p<0.01
NES= 2.22
p<0.01
MPP4
C
KOSP1
KOSP2
NES=1.34
P=0.06
NES=2.32
P<0.001
cKO HSC
cKO MPP1
NES=2.18
p<0.001
NES=1.7
P<0.01
cKO MPP2
NES=2.45
p<0.001
NES=2.62
P<0.001
cKO MPP4
D
Upregulated genes in Mettl3 KO mESCs
NES= -1.62
p<0.001
Mettl3 f/f HSC
cKO HSC
E
Upregulated genes in cKO HSC
Downregulated genes in cKO HSC
NES= 3.10
p<0.001
NES= -2.54
p<0.001
Rbm15 KO LSK
WT LSK
F
KEGG Ribosome
NES= 3.4
FDR= 0.0001
Mettl3 f/f MPP1
HSC
G
6 weeks post transplant
Donor cells
CD45.2 Chimerism %
f/f-HSC
f/f-MPP1
cKO-HSC
cKO-MPP1
B cells
T cells
Gran
Compartments in recipients
H
6 weeks post transplant
Donor cells
LSK
MPP2
MPP4
Compartments in recipients
I
40 weeks post transplant
Donor cells
Pan
Gran
Ery
Mgk
Immature B
PreProB
T cell
Compartments in recipients
J
Upregulated genes in cKO HSC
NES= 1.76
p<0.001
Mettl3 f/f MPP2
HSC
Downregulated genes in cKO HSC
NES= -2.54
p<0.001

Figure S5

Supplementary Figure 5. HSC identity is altered in *Mettl3 cKO* mice. Related to Figure 5.

(A) Unsupervised clustering of differentially expressed genes in three replicates of *Mettl3 f/f* and *Mettl3 cKO* HSC, MPP1, MPP2 and MPP4 cells were shown. **(B)** *Mettl3 cKO* specific clusters are *cKO* HSC-like based on gene expression. GSEA analysis of *cKO* specific cell clusters gene sets (top 50 expressed genes from scRNA-seq) against rank lists of differentially expressed genes between *Mettl3 cKO* HSCs and cKO *MPPs*. **(C)** GSEA analysis with top expressed genes in *cKO* specific cell clusters from scRNA-seq showing the signature of genes enriched in *Mettl3 f/f* HSCs. **(D)** *Mettl3* KO ESC signature is enriched in *Mettl3 cKO* HSCs. Gene Set Enrichment Analysis of upregulated genes in *Mettl3* KO mESCs against the ranklist of differentially expressed genes between *Mettl3 f/f* and *Mettl3 cKO* HSCs. Normalized enrichment score and p value are shown. **(E)** Gene-set enrichment for up or down regulated genes in *Mettl3 cKO* HSCs, as compared to differentially expressed genes in RBM15 KO LSK cells. Normalized enrichment score and FDR are shown. **(F)** *Mettl3 f/f* MPP1 was enriched in KEGG ribosome gene set in regulating translation compared to *Mettl3 f/f* HSCs. **(G-I)** HSCs and MPP1s from cKO mice fail to engraft in recipient mice in a competitive manner. Sorted HSCs and MPP1s from *Mettl3* f/f and *Mettl3* cKO mice were injected into CD45.1 recipient mice competitively with normal CD45.1 BM cells. **(G)** CD45.2 chimerism was shown in peripheral blood at 4 weeks post transplantation. n=10. **(H)** CD45.2 chimerism analysis to show donor engraftment in LSK, MPP2 and MPP4 compartments. n=10. **(I)** Engraftment of CD45.2 donor cells was analyzed in lineage compartments from recipient mice at 40 weeks. n=10. **(J)** Gene-set enrichment analysis plots of up or down regulated genes in *Mettl3 cKO* HSC identified by bulk RNA-seq, against the rank list of differentially expressed genes between *Mettl3 f/f* HSC and *Mettl3 f/f* MPP2. Mean and SEM are shown (*, $P < 0.05$; **, $P < 0.01$; ***, $P < 0.001$, ****, $P < 0.0001$).

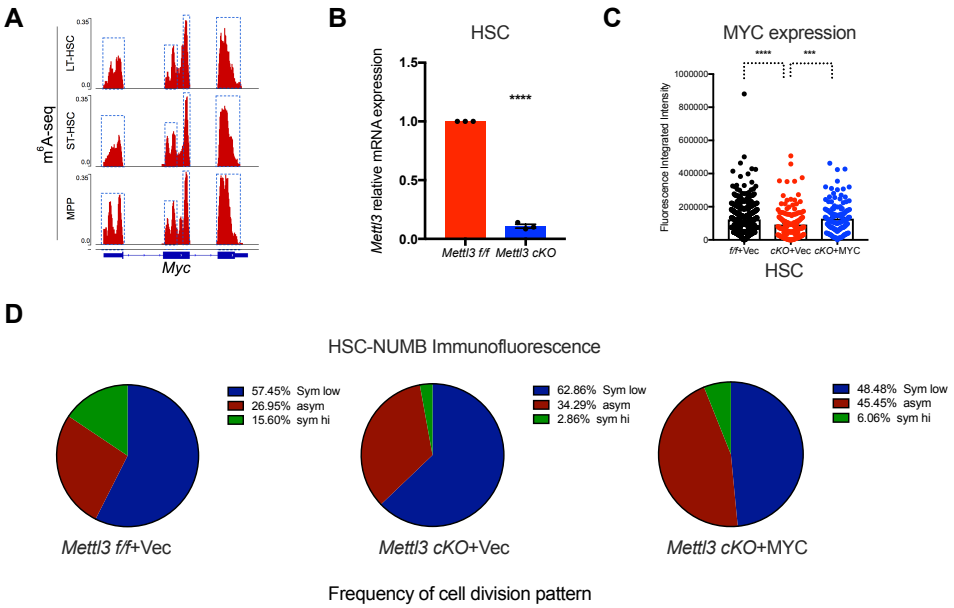
A
LT-HSC
ST-HSC
MPP
m6A-seq
Myc
B
HSC
Mettl3 relative mRNA expression
****
Mettl3 f/f
Mettl3 cKO
C
MYC expression
****
***
Fluorescence Integrated Intensity
f/f+Vec
cKO+Vec
cKO+MYC
HSC
D
HSC-NUMB Immunofluorescence
57.45% Sym low
26.95% asym
15.60% sym hi
Mettl3 f/f+Vec
62.86% Sym low
34.29% asym
2.86% sym hi
Mettl3 cKO+Vec
48.48% Sym low
45.45% asym
6.06% sym hi
Mettl3 cKO+MYC
Frequency of cell division pattern

Figure S6

Supplementary Figure 6. m^{6}A-mediated *Myc* regulation is essential for HSC asymmetric and symmetric cell division. **Related to Figure 6.**

(A) m^{6}A marks on *Myc* transcripts in HSCs and MPPs. m^{6}A peaks were indicated in dot line square. **(B)** qRT-PCR of *Mettl3* in *Mettl3 f/f* and *Mettl3 cKO* HSCs. **(C,D)** Overexpression of MYC in *Mettl3 cKO* HSCs partially rescued HSC symmetric commitment defect in pair daughter assay as quantified by immunofluorescence. Number of daughter pairs assessed: *Mettl3 f/f* +Vec, n=141; *cKO*+Vec, n=35; *cKO*+MYC, n=33.

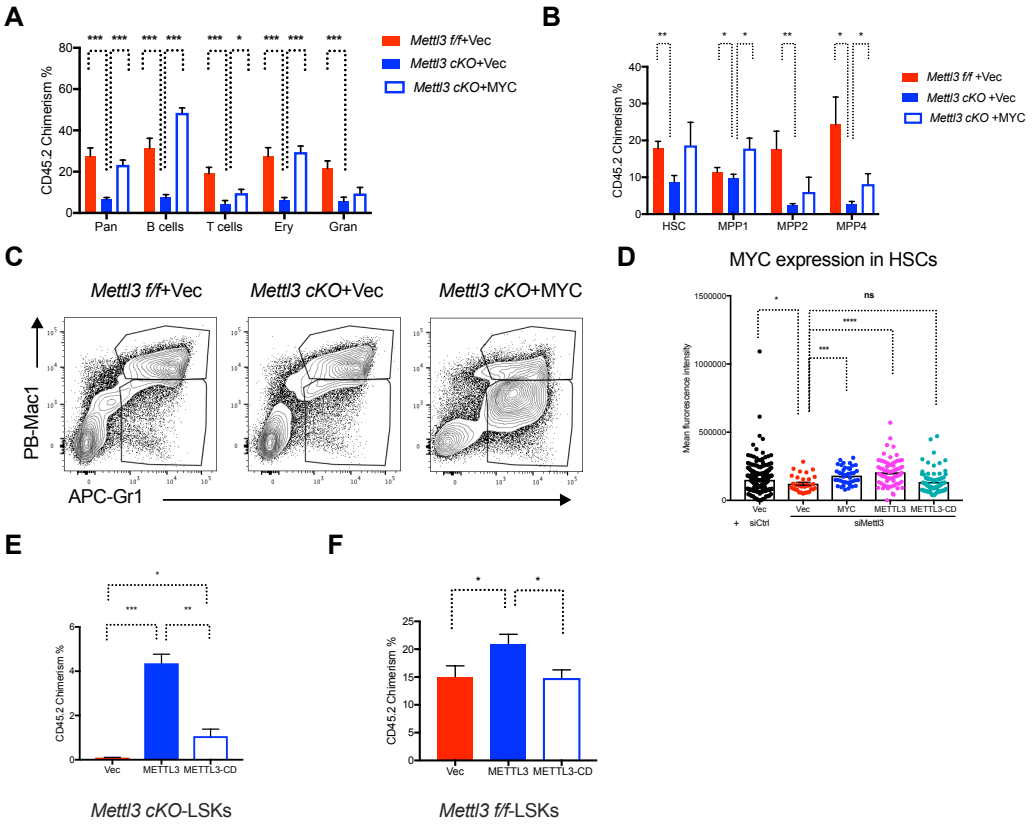
A
CD45.2 Chimerism %
Pan
B cells
T cells
Ery
Gran
Mettl3 f/f+Vec
Mettl3 cKO+Vec
Mettl3 cKO+MYC
B
CD45.2 Chimerism %
HSC
MPP1
MPP2
MPP4
Mettl3 f/f +Vec
Mettl3 cKO +Vec
Mettl3 cKO +MYC
C
Mettl3 f/f+Vec
Mettl3 cKO+Vec
Mettl3 cKO+MYC
PB-Mac1
APC-Gr1
D
MYC expression in HSCs
Mean fluorescence intensity
Vec
MYC
METTL3
METTL3-CD
siCtrl
siMettl3
E
CD45.2 Chimerism %
Vec
METTL3
METTL3-CD
Mettl3 cKO-LSKs
F
CD45.2 Chimerism %
Vec
METTL3
METTL3-CD
Mettl3 f/f-LSKs

Figure S7

Supplementary Figure 7. METTL3 and MYC partially rescue defect in *Mettl3 cKO* HSCs. Related to Figure 7.

(A-C) Sorted control or *Mettl3 cKO* LSK cells transduced with control or MYC overexpression retrovirus and then transplanted into recipient mice. **(A)** Engraftment of donor-derived CD45.2 cells in different lineage cells including B cells(B220+), T cells (CD3+), Erythroblast (Ter119+) and Granulocyte (Gr1+). n=10. **(B)** Engraftment of donor-derived CD45.2 cells in HSC and MPP compartments in recipient mice BM. n=10. **(C)** Representative flow cytometry plots to show abnormal myeloblast in recipient mice transplanted with MYC overexpressed *Mettl3 cKO* LSKs. **(D)** Sorted HSCs were co-transfected with control or *Mettl3* siRNA together with empty vector or MYC, METTL3, METTL3-CD constructs as indicated in the figure. Overall MYC expression is quantified by immunofluorescence. **(E)** LSK cells were sorted from *Mettl3 cKO* mice and transduced with control or wild-type METTL3 or catalytically dead METTL3 (METTL3-CD) overexpression retrovirus. Donor cells were then transplanted into CD45.1 recipient mice with CD45.1 competitor BM cells. CD45.2 chimerism was shown in peripheral blood at 4 weeks post transplantation. n=5. **(F)** Sorted *Mettl3 f/f* LSK cells were transduced with a retrovirus expressing GFP together with an empty vector as control, or a retrovirus expressing METTL3 or METTL3-CD and then transplanted into recipient mice. CD45.2 donor engraftment was analyzed at 4 weeks post-transplant. n=10. Mean and SEM are shown (*, $P < 0.05$; **, $P < 0.01$; ***, $P < 0.001$, ****, $P < 0.0001$).